Materials Advances

ROYAL SOCIETY OF CHEMISTRY

PAPER

View Article Online
View Journal | View Issue

Check for updates

Cite this: *Mater. Adv.*, 2024, **5**, 1648

TiO_2 core–shell and core-dual-shell nanoparticles with tunable heterojunctions and visible to near-infrared extinctions†

Riddhiman Medhi,[a] Sarawut Plengjaroensirichai,[b] Nhat Ngo,[b] Maria D. Marquez,[b] Pannaree Srinoi,[c] Hung-Vu Tran,[d] Allan J. Jacobson,[b] Tai-Chou Lee[e] and T. Randall Lee *[b]

Received 25th September 2023,
Accepted 5th December 2023

DOI: 10.1039/d3ma00756a

rsc.li/materials-advances

The popular use of titanium dioxide (TiO_2) among metal oxides in a variety of optoelectronic applications can be attributed to its low cost and strong extinction in the UV region. However, TiO_2 suffers from an inability to utilize a major part of the solar spectrum, and from rapid electron–hole recombination of photo-generated charge carriers. These challenges can be resolved by incorporating gold–silver nanoshells (GS–NS) with localized surface plasmon resonances (LSPR) into TiO_2 nanostructures, with the overall goal of understanding near-field LSPR activation as well as electron-transfer and charge-trapping characteristics in core–shell and core-dual-shell systems. A method for the synthesis of core–shell nanoparticles consisting of a hollow gold–silver nanoshell core with a TiO_2 shell (GS–NS@TiO_2) is presented. Synthesis of core-dual-shell nanoparticles with either a semiconducting or insulating interlayer between the GS–NS core and TiO_2 shell (GS–NS@SnO_2@TiO_2 and GS–NS@SiO_2@TiO_2) is also presented. In addition to a strong tunable surface plasmon resonance in the visible to near-IR region that allows better utilization of the solar spectrum by the TiO_2 shell, incorporation of a GS–NS core leads to significant suppression of electron–hole recombination processes in TiO_2, further demonstrating the advantages of the plasmonic core and metal oxide shell architecture. The near-field LSPR properties and charge transfer characteristics were further modified by the incorporation of SnO_2 or SiO_2 interlayers, with the SnO_2 interlayer providing the most effective suppression of charge recombination. Reliable methods to fabricate composite TiO_2-based nanoparticles with finely tunable optical and electrical properties are reported.

1. Introduction

Wide band gap (2–4 eV) metal oxide semiconductors are important materials for the fabrication of transparent electronics, thin-film transistors (TFTs), acoustic devices, solar cells, light-emitting diodes (LEDs), and sensors.[1–11] With the demand for these materials expanding rapidly, especially in the field of photocatalysis, the cost-effective fabrication of materials in the form of nanoscale colloidal particles, is an important task.[7] Recently, metal oxide nanoparticles have been shown to be very effective materials for photocatalytic applications like water splitting, hydrogen generation, CO_2 reduction, degradation of dyes, organic and industrial pollutants, as well as for antibacterial treatment.[5,7] For photocatalysis, which is primarily a surface process, a higher surface area per mass of material becomes a critical factor for commercial utilization. In addition to their deposition as finely structured thin films, colloidal nanoparticles also offer flexibility for use in suspensions, colloidal solution-phase reactions, and incorporation within

---

[a] Department of Chemistry, University of Scranton, 800 Linden Street, Scranton, Pennsylvania 18510, USA
[b] 5004 SERC, Department of Chemistry and the Texas Center for Superconductivity, University of Houston, 4800 Calhoun Road, Houston, Texas 77204-5003, USA. E-mail: trlee@uh.edu; Fax: +1 (281) 754-4445; Tel: +1 (713) 743-2724
[c] Department of Chemistry, Faculty of Science, Kasetsart University, Bangkok 10900, Thailand
[d] NTT Hi-Tech Institute, Nguyen Tat Thanh University, 298-300A Nguyen Tat Thanh Street, District 4, Ho Chi Minh City 7280, Viet Nam
[e] Department of Chemical and Materials Engineering, National Central University, 300 Jhongda Road, Jhongli City 32001, Taiwan

† Electronic supplementary information (ESI) available: Additional experimental details, materials used and characterization methods; synthesis scheme and SEM images for Ag NPs and GS-NSs; additional TEM images, STEM-EDX spectra and STEM-EDX line spectra for GS-NS@TiO_2(×2), GS-NS@SnO_2@TiO_2(×2), and GS-NS@SiO_2@TiO_2(×2) NPs; are included in the Supplementary Data. See DOI: https://doi.org/10.1039/d3ma00756a

polymeric structures.[12–16] Titanium dioxide (TiO_2) is the earliest discovered and most widely used metal oxide photocatalyst by virtue of its low cost, low toxicity, high photoactivity, and good chemical and thermal stability.[17] Like many other metal oxides, however, TiO_2 faces two major challenges to widespread practical use in solar light-induced photocatalytic and photovoltaic applications. The first limitation is its inability to utilize the majority of the solar spectrum that reaches the earth's surface; due to its wide band gap, extinction is limited to the UV region only.[17] The second limitation for TiO_2 is the poor quantum yield caused by rapid recombination of photogenerated electrons and holes.[16–18]

Noble metal nanoparticles are a class of materials known for strong extinction of light in visible to near-IR regions. Localized surface plasmon resonance (LSPR) leads to strong extinction of light with a frequency matching that of the oscillating electrons in the nanoparticle. In noble metal nanoparticles, these resonances correspond to strong extinctions in the visible and near-IR wavelengths.[19–21] Gold nanoparticles (Au NPs) are the most commonly used type of materials for this purpose, with their extinction in the range between 520–560 nm.[19,22] This LSPR extinction can be extended towards the longer wavelengths by changing the morphology to nanorods, nanocubes, nanostars, nanoshells, or nanospheres of larger sizes.[23–27] Various types of gold nanoparticles have been studied in core–shell systems with TiO_2 and have effectively enhanced their visible-light photoactivity.[27–32] Recently, hollow nanoshells of gold alloyed with silver (GS–NS) were demonstrated to be a much more stable alternative to gold nanoparticles, affording a wider LSPR signal using lesser and cheaper material.[33] The extinction of GS–NS is tunable across the entire range between 500–1000 nm.[16] In a previous paper, our groups showed that incorporating a GS–NS core inside a SnO_2 shell can activate intense extinction of light in visible and near-IR regions.[34] Additionally, the GS–NS core led to a remarkable near-complete suppression in the rate of electron–hole recombination in the SnO_2 shell; demonstrating the distinct advantages of the metal core- metal oxide shell architecture.

Encouraging results observed with SnO_2 suggests that GS–NSs could have a similar potential to overcome the limitations of TiO_2 as well. SnO_2 and TiO_2 are similar in terms of their crystal structure (rutile and anatase) and bond lengths ($\sim$1.9 Å), giving rise to comparable band gaps ($\sim$3.2–3.6 eV).[35,36] However, the optical and electronic properties can be quite different. Theoretical studies of their electronic structures (both rutile and anatase) show that the conduction band (CB) of TiO_2 has several dense energetically flat levels, while the CB of SnO_2 has a single highly dispersive level.[35] As a consequence, TiO_2 absorbs UV wavelengths much more strongly compared to SnO_2. To add to the strong UV extinction, this work attempts to utilize the properties of a GS–NS core with metal oxide shell architecture for enhancing visible and near-IR utilization and charge separation of TiO_2. Most recipes for uniform TiO_2 nanoparticle synthesis involve controlled hydrolysis of titanium alkoxides in non-aqueous solvents.[37–41] This route is typically preferred because titanium alkoxides spontaneously hydrolyze to form TiO_2 when exposed to water, hence controlled growth of TiO_2 shells cannot be performed in an aqueous environment.[37–41] However, most popular methods for plasmonic noble metal nanoparticle synthesis involve aqueous systems.[16,42–45] This report describes an effective synthetic strategy to circumvent this problem to achieve the controlled growth of TiO_2 shells with various thickness around plasmonic GS–NS cores.

In addition to noble metal nanoparticle coupling, other strategies explored to increase electron–hole pair separation efficiency in TiO_2 are nanoscale heterostructures with other semiconductors, which have received attention due to their excellent charge separation and catalytic activities.[46,47] Among the semiconductor/TiO_2 heterojunction systems, the SnO_2/TiO_2 heterostructure attracts interest in particular due to their structural analogy. Both oxides have the same crystal symmetry (tetragonal) and have two molecular units per unit cell ($Z = 2$).[46] SnO_2 and TiO_2 form a type-II heterojunction. The valence band (VB) of TiO_2 is energetically positioned between the VB and CB of SnO_2, while the CB of TiO_2 is positioned above the VB and CB of SnO_2.[46] When activated simultaneously, this staggered conformation of energy levels means that the CB of SnO_2 can act as a sink for photogenerated electrons.[46] The photogenerated holes move in the opposite direction and accumulate in the VB of TiO_2. This formation of an excitonic charge separation state leads to an effective separation of electrons and holes, reducing recombination.[48] This feature is beneficial to applications such as photovoltaic devices and photocatalysts. The SnO_2/TiO_2 core–shell heterojunction characteristics have been extremely effective for dye-sensitized solar cells due to an effective inhibition of back-electron transfer between the oxidized dye and reduced semiconductor.[47,49,50] So far, such metal oxide heterojunctions have been mostly fabricated and studied as thin films, and nanowire arrays.[46,51] In this current study, a strategy to synthesize this heterojunction in a colloidal nanoparticle is described. Previously, our group has synthesized the TiO_2/SnO_2 heterojunction with TiO_2 as the core and SnO_2 as the shell, making a reduction photocatalyst material, with electrons collecting at the outer SnO_2 shell.[36] The nanoparticles reported in this paper feature the reverse heterojunction, employing a TiO_2 shell outside a SnO_2-based core which would concentrate holes on the TiO_2 shell outside, making them more effective as an oxidation photocatalyst. Photogenerated holes oxidize hydroxide ions to hydroxide radicals which act as the major oxidizing species in oxidation photocatalysis.[51] Importantly, in this report, a three-layer composite with TiO_2 shells around a plasmonic GS–NS with a SnO_2 interlayer is synthesized to generate the plasmonically-activated SnO_2/TiO_2 heterojunction core-dual-shell nanoparticle - GS–NS@SnO_2@TiO_2.

According to a previous report by Li *et al.*, photocatalytic activation in $ZnIn_2S_4$ was greatly enhanced by incorporating a GS–NS core, which was further improved by the presence of an insulating SiO_2 interlayer.[16] As a different kind of dielectric to SnO_2, an insulating SiO_2 interlayer is expected to block electron movement between the TiO_2 shell and GS–NS core. However, there is no direct evidence in the literature to confirm this hypothesis. To study this effect, GS–NS@SiO_2@TiO_2

nanoparticles were also synthesized. A facile and versatile method is reported herein for the controlled growth of TiO_2 shells directly on a metal core such as GS–NSs, as well as on GS–NSs with an insulating (SiO_2) and semiconducting (SnO_2) interlayers. The effects of the different interlayers on the near-field LSPR properties and charge transfer between the GS–NS core and TiO_2 shell has been investigated. A better understanding of these different types of interlayers in such a system adds an extra degree of control in tuning the optical and electrical properties on the nanoscale. All of the nanoparticles were characterized by scanning electron microscopy (SEM), transmission electron microscopy (TEM), scanning transmission electron microscopy (STEM), energy dispersive X-ray spectroscopy (EDX), X-ray photoelectron spectroscopy (XPS), and X-ray diffraction (XRD). Separately, the optical properties were evaluated by UV-vis spectroscopy and the rates of electron–hole recombination in these various TiO_2-based systems were compared using photoluminescence spectroscopy (PL).

2. Materials and methods

2.1. Synthesis of hollow gold–silver nanoshells (GS–NS)

Hollow gold–silver nanoshells (GS–NS) were prepared as outlined in Scheme S1 (ESI†), using the recipe previously reported by our group.[34] After removing the supernatant, the residue was redispersed in 10 mL of Milli-Q water.

2.2. Synthesis of GS–NS@TiO_2 core–shell nanoparticles

The TiO_2 coating recipe, outlined in Scheme 1, is a modification of the recipe reported by Lee *et al.*[52] The first step is phase-transfer of the GS–NSs to an ethanol solvent. Specifically, 0.02 g of hydroxypropyl cellulose (HPC) was added to a 10 mL solution of GS–NSs in Milli-Q-water from the previous step and sonicated for 90 min for functionalization. After functionalization with HPC, 15 mL of EtOH was added to this dispersion, sonicated again for 10–15 min, and then centrifuged at 8000 rpm for 15 min. The supernatant was discarded, 15 mL of EtOH was added, and the solution sonicated again for 15 min. To reduce or eliminate the formation of unwanted TiO_2 from hydrolysis of TBOT in free solution, anhydrous EtOH from a freshly opened bottle was used at each step. This solution was then centrifuged at 8000 rpm for 15 min, the supernatant was discarded to remove any remaining water, and then finally redispersed in 1 mL of EtOH.

Subsequently, this concentrated solution of GS–NSs in EtOH was transferred to a glass vial, and 0.02 g of HPC was added. To activate the controlled hydrolysis of TBOT, 300 μL of Milli-Q-water was also added to this vial, and the contents were sonicated for 90 min. Subsequently, 180 μL (0.528 mmol) of TBOT was dissolved in 4 mL of EtOH from a freshly opened bottle. Using a syringe pump, 3 mL of this TBOT solution was then slowly added to the HPC-functionalized GS–NSs over 30 min under stirring. The reaction vial was then stirred overnight at rt. The contents of the reaction vial were then transferred to a 75 mL round-bottom flask and refluxed at 85 °C for 90 min. The contents were then cooled to rt and centrifuged, typically at 8000 rpm for 15 min, washed with EtOH, centrifuged again, and finally redispersed in 1 mL of EtOH. The nanoparticles thus obtained after the first TiO_2 coating are denoted as GS–NS@TiO_2(×1). To increase the thickness of the TiO_2 shell, a second coating was performed on the GS–NS@TiO_2(×1) nanoparticles. Specifically, 0.02 g of HPC was added to 1 mL of GS–NS@TiO_2(×1) and sonicated for 90 min. Subsequently, 180 μL (0.528 mmol) of TBOT was dissolved in 4 mL of EtOH from a freshly opened bottle. Using

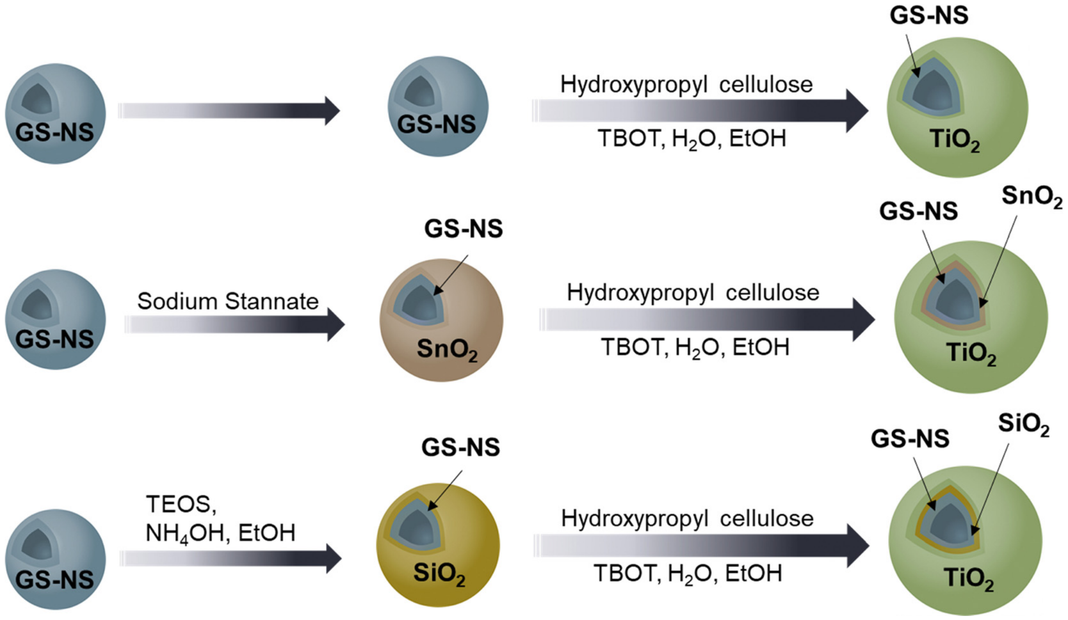

Scheme 1 Synthesis route for GS–NS@TiO_2, GS–NS@SnO_2@TiO_2, and GS–NS@SiO_2@TiO_2 nanoparticles.

a syringe pump, 3 mL of this TBOT solution was then slowly added to the HPC-functionalized GS–NSs over 30 min under stirring. The reaction was stirred overnight at rt, then the contents were transferred to a 75 mL round-bottom flask and refluxed at 85 °C for 90 min. The contents were then cooled to rt and centrifuged, typically at 8000 rpm for 15 min, washed twice with EtOH, centrifuged again, and finally redispersed in 1 mL of EtOH. The nanoparticles thus obtained after the second TiO_2 coating are denoted as GS–NS@TiO_2(×2).

2.3. Synthesis of GS–NS@SnO_2 core–shell nanoparticles

As outlined in Scheme 1, the recipe reported previously by our group was used to synthesize the SnO_2-coated GS–NS.[34] The particles were washed once after synthesis and finally redispersed in 10 mL of Milli-Q water.

2.4. Synthesis of GS–NS@SiO_2 core–shell nanoparticles

The SiO_2 coated GS–NS were adapted from a previously reported method, as outlined in Scheme 1.[16] Briefly, 10 mL of the GS–NS solution was diluted to 20 mL and added to a 150 mL round bottom flask. Separately, 2 mL of ammonium hydroxide was mixed with 45 mL of fresh ethanol and this mixture was added to the flask containing the diluted GS–NS solution. After 10 min of stirring, 35 μL of TEOS was added to this mixture and stirred overnight at rt. The contents were then centrifuged at 8000 rpm for 15 min, the supernatant was discarded, and the residue was redispersed in 10 mL of ethanol.

2.5. Synthesis of GS–NS@SnO_2@TiO_2 and GS–NS@SiO_2@TiO_2 core-dual-shell nanoparticles

The recipe for phase transfer of GS–NS@SnO_2 core is similar to that for the GS–NS core after HPC functionalization, as outlined in Scheme 1. Specifically, 10 mL of the GS–NS@SnO_2 in water from the previous step was taken, 15 mL of EtOH was added to this dispersion, sonicated for 10–15 min, and then centrifuged at 8000 rpm for 15 min. The supernatant was discarded, 15 mL of EtOH was added, and the solution sonicated again for 15 min. This solution was then centrifuged again at 8000 rpm for 15 min, the supernatant was discarded to remove any remaining water and then finally redispersed in 1 mL of EtOH. The phase transfer of the GS–NS@SiO_2 core is simpler since the nanoparticles are already dispersed in EtOH. Specifically, 10 mL of the GS–NS@SiO_2 in EtOH from the previous step was concentrated by centrifuging and directly redispersing into 1 mL of EtOH. After generating a concentrated solution of GS–NS@SnO_2 or GS–NS@SiO_2 in EtOH, the TiO_2 coating recipe is exactly the same as described for the GS–NS core. The nanoparticles thus obtained after the first TiO_2 coating are denoted as GS–NS@SnO_2@TiO_2(×1) and GS–NS@SiO_2@TiO_2(×1), while those obtained after the second TiO_2 coating are denoted as GS–NS@SnO_2@TiO_2(×2) and GS–NS@SiO_2@TiO_2(×2), respectively.

2.6. Synthesis of GS–NS@SiO_2@TiO_2-seed nanoparticles

The recipe for GS–NS@SiO_2@TiO_2 nanoparticles is modified to synthesize GS–NS@SiO_2 nanoparticles decorated with TiO_2-seeds. Specifically, 10 mL of the GS–NS@SiO_2 in EtOH from the previous step was concentrated by centrifuging and redispersed into 1 mL of EtOH. This concentrated solution of GS–NS@SiO_2 in EtOH was transferred to a glass vial and 0.02 g of HPC was added. To activate the controlled hydrolysis of TBOT, 50 μL of Milli-Q-water was also added to this vial, and the contents were sonicated for 90 min. Subsequently, 60 μL (0.176 mmol) of TBOT was dissolved in 4 mL of EtOH from a freshly opened bottle. Using a syringe pump, 3 mL of this TBOT solution was then slowly added to the HPC-functionalized GS–NS@SiO_2 over 30 min under stirring. The reaction vial was then stirred for 90 min at rt. The contents of the reaction vial were transferred to a 75 mL round-bottom flask and refluxed at 85 °C for 90 min. The reaction mixture was allowed to cool down to rt and then sonicated for 90 min. The contents were then centrifuged, typically at 8000 rpm for 15 min, and finally redispersed in 1 mL of EtOH. The nanoparticles thus obtained after the TiO_2 seeding are denoted as GS–NS@SiO_2@TiO_2-seed nanoparticles. This seeding recipe can be repeated again to increase the number of TiO_2 seeds on the surface.

3. Results and discussion

3.1. Synthesis and morphological study of the nanoparticles

3.1.1. Gold silver nanoshells (GS–NSs). The hollow gold–silver nanoshells (GS–NSs) were prepared in two steps as described in our previous paper[34] and illustrated in Scheme S1 (ESI†). Silver nanoparticles with diameter ∼30–50 nm (SEM image in Fig. S1a, ESI†) were prepared in the first step. Once the Ag NPs were obtained, hollow gold–silver nanoshells (GS–NSs) were generated by performing a galvanic replacement to reduce gold onto the silver nanoparticles, using a K-gold solution comprising of $HAuCl_4$ and K_2CO_3, described in detail on our previous paper.[34] To obtain the exact desired extinction maximum for each batch of GS–NSs, the reaction was monitored using UV-Vis spectroscopy, resulting in slight variations in the reaction time. The optical properties are discussed in detail in later sections. The SEM images (Fig. S1b, ESI†) confirm the successful formation of hollow spherical gold–silver nanoshells. As determined from size measurements, the average diameter of the GS–NSs was 56 ± 9 nm.

3.1.2. GS–NS@TiO_2 core–shell nanoparticles. After the successful synthesis of GS–NSs, titanium dioxide shells were grown around these nanoparticles, as outlined in Scheme 1. The synthesis strategy to grow the TiO_2 shells is loosely based on the method reported by Lee *et al.*[52] The TiO_2 shells are formed by the hydrolysis of titanium butoxide (TBOT). TBOT spontaneously hydrolyses to titanium dioxide when it comes in contact with water and air.[52] To selectively grow TiO_2 only on the surface of the core nanoparticles, a non-aqueous solvent is required, such as ethanol. However, the most popular recipes for the synthesis of various noble metal nanoparticles like Au and Ag NPs, are based on the sodium citrate method in water.[16,42–45] The GS–NSs described in this manuscript are also citrate stabilized in water. Furthermore, these Au NPs, Ag NPs, as well as GS–NSs spontaneously aggregate when dried or when dispersed in ethanol and other non-aqueous solvents, which poses a challenge when adopting the alkoxide hydrolysis method to grow TiO_2 shells on such plasmonic cores. Addition of TBOT to such an aqueous solution of plasmonic nanoparticles leads to the formation of large amounts of TiO_2 in free solution rather than growing exclusively on the surface of the plasmonic core. To circumvent this problem, the need for a stabilizing surfactant to enable dispersibility in ethanol for the GS–NS is crucial. However, since the GS–NSs also aggregate when dried, the GS–NS require colloidal functionalization with the new surfactant first in water and then redispersed into ethanol.

In this report, hydroxypropyl cellulose (HPC) was chosen as the surfactant. In addition to successful phase transfer, hydroxypropyl cellulose can also stabilize and disperse the final TiO_2 coated core–shell composites synthesized by hydrolysis of TBOT in ethanol.[52] Lee *et al.* compared the growth of TiO_2 shells on SiO_2 cores from TBOT with and without HPC and found that the addition of HPC significantly improves the dispersion of the final nanoparticles.[53] Although, eccentric TiO_2-coated Au nanostructures were obtained by Seh *et al.* using HPC,[54] our goal is to synthesize uniform shells of TiO_2 onto gold–silver alloy systems and such uniform shells require the use of TBOT as the TiO_2 precursor.[52] Thus, in our method we attempted to exploit the dual-ability of HPC as a phase-transfer agent as well as a stabilizer and combine it with the attributes of TBOT hydrolysis to generate uniform TiO_2 shells around aqueously synthesized metal nanoparticles. The GS–NS solution functionalized with HPC, was washed with anhydrous ethanol multiple times to eliminate water. Secondly, the as-prepared HPC-functionalized GS–NS solutions were concentrated 10-fold due to the need for a high NP concentration to reduce free solvent volume further, diminishing the chances for formation of free TiO_2. A minimal amount of Milli-Q water was then added to the concentrated core nanoparticle solution along with hydroxypropyl cellulose and sonicated to selectively disperse the HPC and water molecules on the surface of the GS–NSs. The slow addition of TBOT precursor and overnight stirring followed by reflux leads to the formation of TiO_2 shells *via* controlled hydrolysis.

The SEM and TEM images demonstrate the successful formation of TiO_2 shells around the GS–NSs. As evident from the SEM image in Fig. 1, TiO_2 is exclusively hydrolyzed only on the surface of the GS–NS, and the formation of free TiO_2

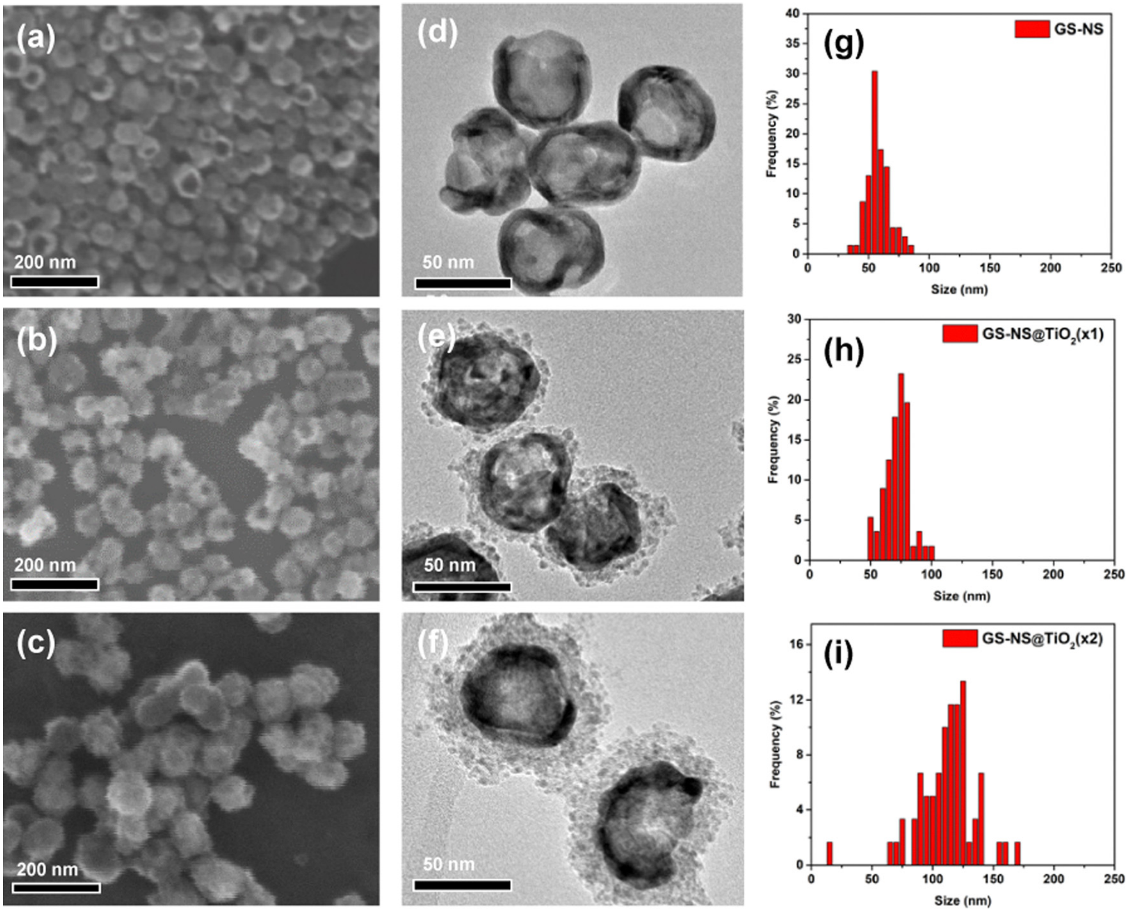

Fig. 1 (a)–(c) SEM images, (d)–(f) TEM images, and (g)–(i) Size distribution histograms for GS–NSs, GS–NS@TiO_2(×1), and GS–NS@TiO_2(×2) nanoparticles, respectively. The fuzzy appearance of the particles in many of the SEM and TEM images can be attributed to polycrystalline nature of the TiO_2 coatings and the resolution of our microscopy instruments.

particulates is dramatically reduced or completely eliminated. Obtaining a thicker TiO_2 shell in a single step by increasing water or TBOT concentration is complicated by the formation of free TiO_2. Instead, to obtain thicker shells with good uniformity, the coating process is repeated on the already coated nanoparticles. The TEM images in Fig. 1 show that the TiO_2 shell becomes thicker after the second coating. Using statistical image analysis of the SEM images (Table 1), after one coating, the average diameter of the GS–NS@TiO_2(×1) nanoparticles was determined to be 70 ± 10 nm. According to these measurements, the TiO_2 shells have an average thickness of 7 ± 1 nm. After a second coating, the average diameter increased to 112 ± 31 nm, indicating an increase in TiO_2 shell thickness to 28 ± 11 nm for the GS–NS@TiO_2(×2) nanoparticles.

3.1.3. GS–NS@SnO_2 and GS–NS@SiO_2 core–shell nanoparticles. The SnO_2-coated GS–NSs were synthesized according to a previously described method, as outlined in Scheme 1.[34] The SEM image of the SnO_2-coated GS–NSs in Fig. 2a shows that they are all uniformly covered with a thin tin oxide shell. Using statistical image analysis of the SEM images, after one coating, the average diameter of the GS–NS@SnO_2 nanoparticles was determined to be 77 ± 15 nm. According to these measurements, the SnO_2 shells have an average thickness of 11 ± 3 nm. Overall, analysis by SEM showed that the tin oxide coated core–shell nanoparticles were well dispersed, spherical, and uniformly sized (Fig. 2a).

The synthesis procedure for SiO_2 coated GS–NS was adopted from a previously reported method, as outlined in Scheme 1.[16] TEOS was used as the SiO_2 precursor. The thickness of the SiO_2

Table 1 Nanoparticle size and shell thicknesses

Particle	GS–NS core diameter (nm)	SnO_2 shell thickness (nm)	SiO_2 shell thickness (nm)	TiO_2 shell thickness (nm)	Total diameter (nm)
GS–NS	56 ± 9	—	—	—	56 ± 9
GS–NS@TiO_2(×1)	56 ± 9	—	—	7 ± 1	70 ± 10
GS–NS@TiO_2(×2)	56 ± 9	—	—	28 ± 11	112 ± 31
GS–NS@SnO_2	56 ± 9	11 ± 3	—	—	77 ± 15
GS–NS@SnO_2@TiO_2(×1)	56 ± 9	11 ± 3	—	4 ± 1	85 ± 15
GS–NS@SnO_2@TiO_2(×2)	56 ± 9	11 ± 3	—	17 ± 4	110 ± 23
GS–NS@SiO_2	56 ± 9	—	23 ± 7	—	102 ± 22
GS–NS@SiO_2@TiO_2(×1)	56 ± 9	—	23 ± 7	5 ± 4	112 ± 30
GS–NS@SiO_2@TiO_2(×2)	56 ± 9	—	23 ± 7	10 ± 3	122 ± 28

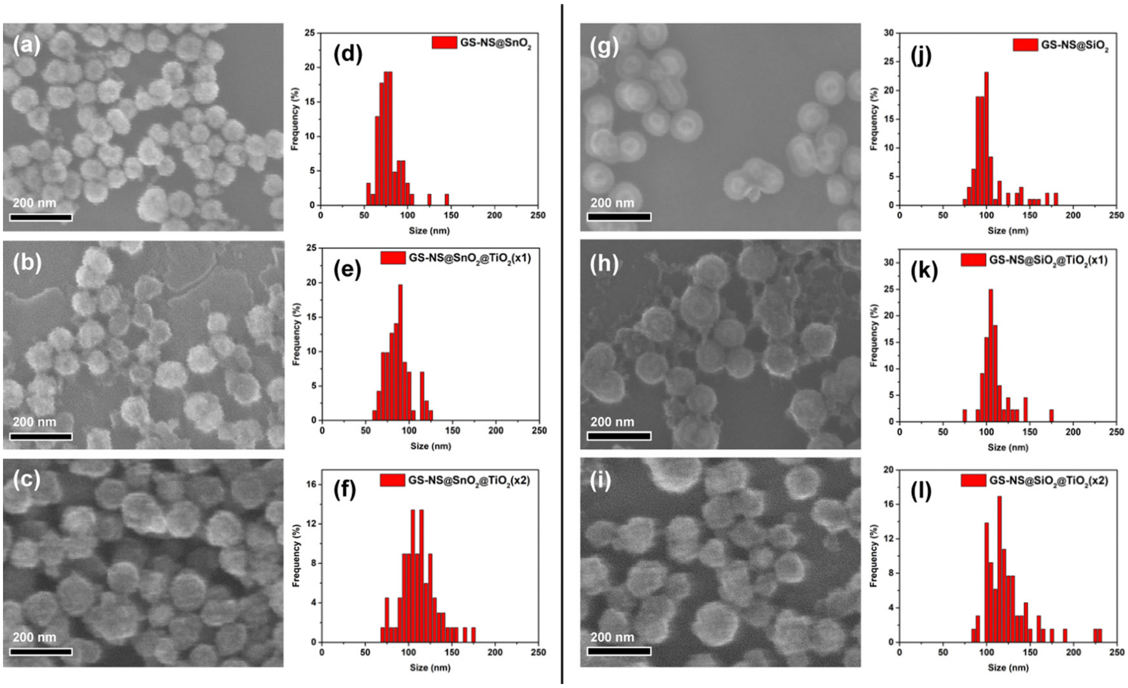

Fig. 2 (a)–(c) SEM images and (d)–(f) Size distribution histograms for stepwise coating of TiO_2 shells on GS–NS cores with a SnO_2 interlayer. (g)–(i) SEM images and (j)–(l) Size distribution histograms for stepwise coating of TiO_2 shells on GS–NS cores with a SiO_2 interlayer. The fuzzy appearance of the particles in many of the SEM and TEM images can be attributed to polycrystalline nature of the TiO_2 coatings and the resolution of our microscopy instruments.

shell can be varied by changing the amount of TEOS. In our experiments, the amount of TEOS was fixed at 35 μL. The SEM image in Fig. 2g shows the morphology of the GS–NS@SiO_2 nanoparticles. Using statistical image analysis of the SEM images, after one coating, the average diameter of the GS–NS@SiO_2 nanoparticles was determined to be 102 ± 22 nm. According to these measurements, the SiO_2 shells have an average thickness of 23 ± 7 nm.

3.1.4. GS–NS@SnO_2@TiO_2 and GS–NS@SiO_2@TiO_2 core-dual-shell nanoparticles. As outlined in Scheme 1, the GS–NS@SnO_2 and GS–NS@SiO_2 cores underwent the same treatment as the GS–NSs to generate TiO_2 core-dual-shell nanoparticles with a semiconducting and insulating interlayer, respectively. The TiO_2 shell is visibly more evident on the GS–NS@SiO_2 core, see Fig. 2 and Fig. S2 (ESI†), as the rough texture of the TiO_2 shell is distinct from the smooth SiO_2 interlayer. The texture of TiO_2 is not so different from that of SnO_2, making it challenging to distinctly differentiate the TiO_2 layer around the SnO_2. However, the TiO_2 shell has a more rugged morphology compared to the SnO_2 shell (see Fig. S2, ESI†). On comparing the texture and total diameter with the GS–NS@SnO_2 nanoparticles, the presence of the TiO_2 shell in GS–NS@SnO_2@TiO_2 becomes evident in Fig. S2 (ESI†). STEM-EDX elemental mapping of Sn and Ti, covered in detail in the next section, further demonstrates the distribution of the SnO_2 and TiO_2 phases. As seen in the SEM image (Fig. 2) and TEM images (Fig. 3 and Fig. S2, ESI†), the TiO_2 shells are fairly uniform and continuous. Once again, there is also very limited formation of free TiO_2 aggregates. Using statistical image analysis of the SEM images (Table 1), after one round of coating, the TiO_2 shells in the GS–NS@SnO_2@TiO_2(×1) nanoparticles exhibited an average thickness of 4 ± 1 nm. A second coating increased the TiO_2 shell thickness to 17 ± 4 nm for the GS–NS@SnO_2@TiO_2(×2) nanoparticles. For the nanoparticles with a SiO_2 interlayer, after one coating, the TiO_2 shells in the GS–NS@SiO_2@TiO_2(×1) nanoparticles exhibited an average thickness of 5 ± 4 nm. After a second coating, the average TiO_2 shell thickness increased to 10 ± 3 nm for the GS–NS@SiO_2@TiO_2(×2) nanoparticles. Thus, this recipe allows one to synthesize SnO_2/TiO_2 and SiO_2/TiO_2 heterojunctions in a colloidal nanoparticle using a solution-based method.

The TiO_2 shell formation process is similar on both the GS–NS@SnO_2 and GS–NS@SiO_2 nanoparticles, with similar shell thicknesses obtained for both sets of nanoparticles. These results suggest that the SnO_2-coated nanoparticles can easily adapt to recipes utilized for SiO_2-coated systems. The TiO_2 shell-growth process on GS–NS@SnO_2 cores is also extremely well controlled under identical reaction parameters. SiO_2 has so far been the go-to shell material for nanoparticle stabilization because of its ability to be further encapsulated by other coating materials. SnO_2, here, demonstrates similar abilities. Both materials are largely transparent to visible light and form amorphous or polycrystalline shells.[55–57] Thus both materials do not block incident visible/near-IR-light and small chemical species from accessing the inner core.[55–57] As observed in our previous paper,[34] the SnO_2 coating recipe is also facile and well-controlled, similar to the recipes for the formation of SiO_2 shells.[58] The SnO_2 shell is also more stable than a SiO_2 shell across a wider range of pH values, which makes them more robust shell materials.[58] This feature allows them to be available for further functionalization that may require basic conditions. Unlike SiO_2, which is an insulator, SnO_2 is a wide band gap semiconductor. Furthermore, the band gap, light extinction, and electrical conductivity of SnO_2 can be carefully tuned *via* doping,[34,56] which would not be possible for SiO_2. Thus, the SnO_2 shell offers a very viable and tunable semiconductor alternative to traditional SiO_2 coatings for nanoparticle stabilization and functionalization.

3.1.5. GS–NS@SiO_2@TiO_2-seed nanoparticles. Our experiments showed that two main factors determine the amount of TiO_2 formed: (1) the amount of TBOT and (2) the amount of water. Smaller amounts of water and TBOT lead to thinner shells. The rate of addition is also critical to avoid the formation of free TiO_2. Slow addition is required to ensure selective growth of TiO_2 on the surface of the NP cores. This method can also be modified to coat the plasmonic core with TiO_2 seeds, instead of a complete shell. Decreasing the concentration of the TBOT precursor solution, as well as the amount of water and reaction time, leads to the synthesis of TiO_2-seed decorated nanoparticles. As shown in Fig. 4a and b, the surface of the GS–NS@SiO_2 nanoparticles is smooth originally, whereas the formation of TiO_2 seeds adds contrast and

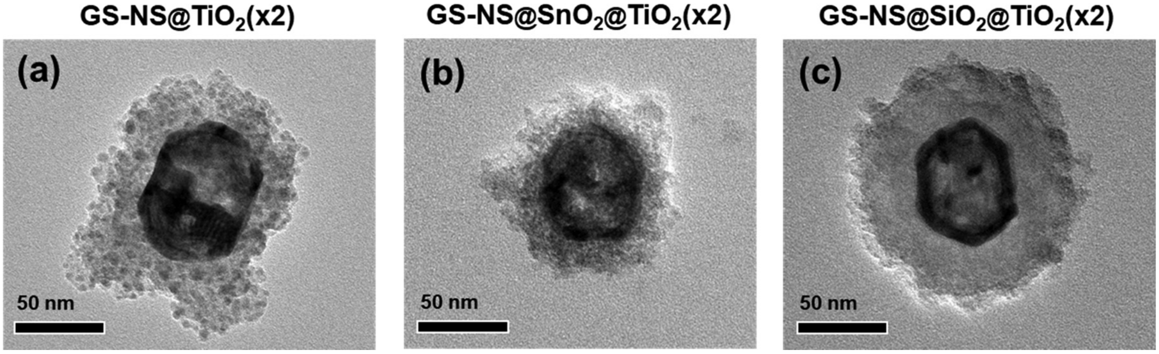

Fig. 3 TEM images of (a) GS–NS@TiO_2(×2), (b) GS–NS@SnO_2@TiO_2(×2), and (c) GS–NS@SiO_2@TiO_2(×2) nanoparticles, respectively.

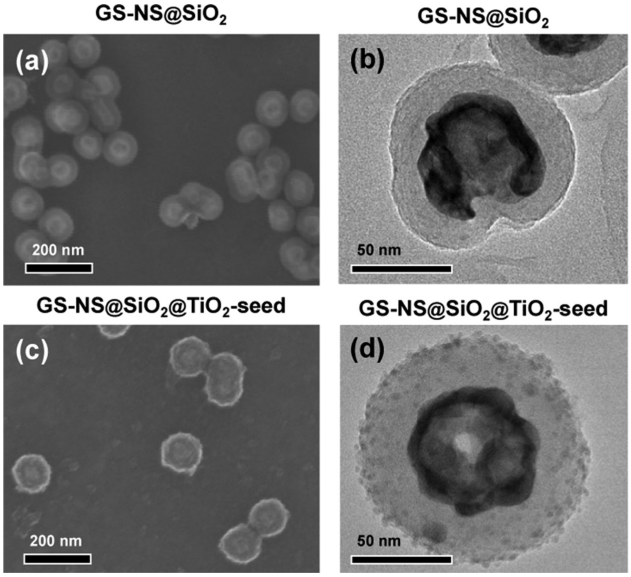

Fig. 4 (a) and (c) SEM images and (b) and (d) TEM images of GS–NS@SiO$_2$ and GS–NS@SiO$_2$@TiO$_2$-seed nanoparticles, respectively.

roughness to the outer surface, as illustrated in Fig. 4c and d. This difference in contrast and roughness between the smooth SiO$_2$ surface and the TiO$_2$-seeded outer surface clearly demonstrates the successful synthesis of GS–NS@SiO$_2$@TiO$_2$-seed nanoparticles.

3.2. Compositional analysis of the nanoparticles

3.2.1. EDX spectroscopy and STEM-EDX mapping. In order to further determine the exact distribution of the elements within the nanoparticles and confirm the core–shell structure, EDX spectroscopy along with elemental mapping and line spectra using STEM-EDX, were performed. As observed in Fig. 5 and Fig. S5–S7 (ESI†), silver and gold are confined only to the inner regions of the nanoparticle. Tin and silicon distributions extend out wider to cover more of the nanoparticle volume, clearly encapsulating the inner gold–silver core in their respective nanoparticles (see Fig. 5 and Fig. S6, S7, ESI†). As shown in Fig. 5 and Fig. S5–S7 (ESI†), the distribution of titanium extends the widest across the nanoparticle volume indicating that this element forms the final outermost shell. The oxygen distribution also mimics the titanium distribution which is consistent with a TiO$_2$ shell. This phenomenon is observed for all three samples of GS–NS@TiO$_2$(×2), GS–NS@SnO$_2$@TiO$_2$(×2), and GS–NS@SiO$_2$@TiO$_2$(×2) nanoparticles (see Fig. 5 and Fig. S5–S7, ESI†).

Fig. S4 (ESI†) shows that the EDX spectra for the final core–shell nanoparticles after two rounds of TiO$_2$ coatings contains the characteristic peaks for Ag, Au, Ti, and Sn/Si in their respective nanoparticles. The relative atomic concentrations of Ag, Au, Si, Ti, and Sn obtained from EDX measurements listed in Table S1 (ESI†), roughly match the relative volume occupied by their corresponding phases in the respective nanoparticle architectures. For example, the relative concentration of Ti is highest in the GS–NS@TiO$_2$(×2) since this nanoparticle has the thickest TiO$_2$ shell. The relative concentrations in GS–NS@SiO$_2$@TiO$_2$(×2) nanoparticles are dominated by the element Si due to the very thick SiO$_2$ shell. The relative concentration of Ag and Au are also the lowest in this particle as it has the thickest overall shell thickness (SiO$_2$ + TiO$_2$). The relative concentration for Ag and Au in GS–NS@SnO$_2$@TiO$_2$(×2) is lower than the particle with no interlayer but higher than the particle with a thicker SiO$_2$ interlayer, in accordance with size measurements. The concentration of Sn is also lower than Ti in this particle since the thickness of the SnO$_2$ interlayer is less than the total thickness of the TiO$_2$ shell.

3.2.2. XPS surface analysis. XPS analysis was performed to determine the elemental composition on the surface of the nanoparticles at each step of the synthetic process. Fig. 6–8

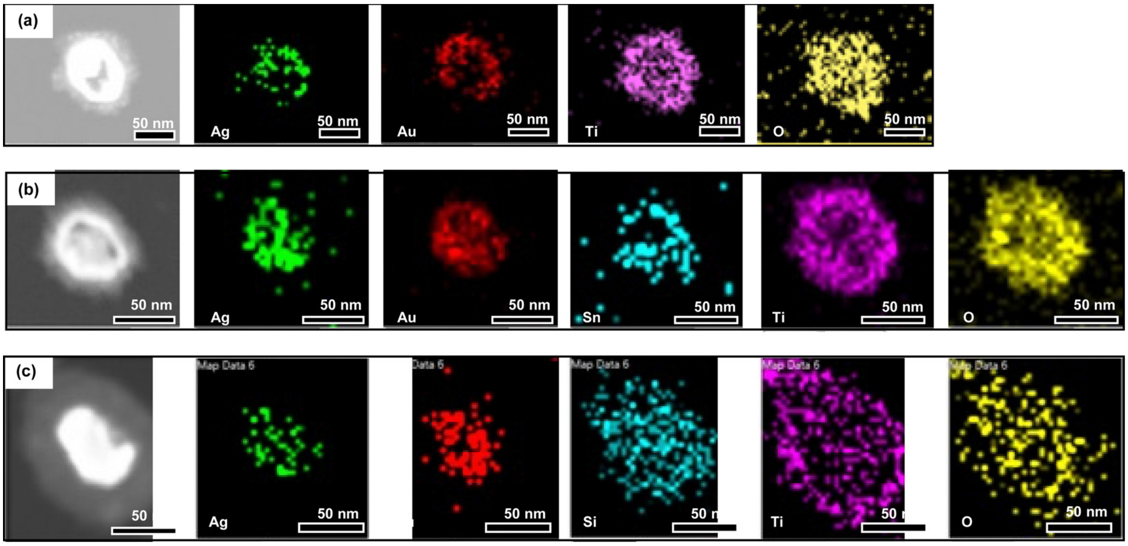

Fig. 5 STEM-EDX mapping images of (a) GS–NS@TiO$_2$(×2), (b) GS–NS@SnO$_2$@TiO$_2$(×2), and (c) GS–NS@SiO$_2$@TiO$_2$(×2) nanoparticles, showing the distribution of the constituent elements in the respective nanoparticles.

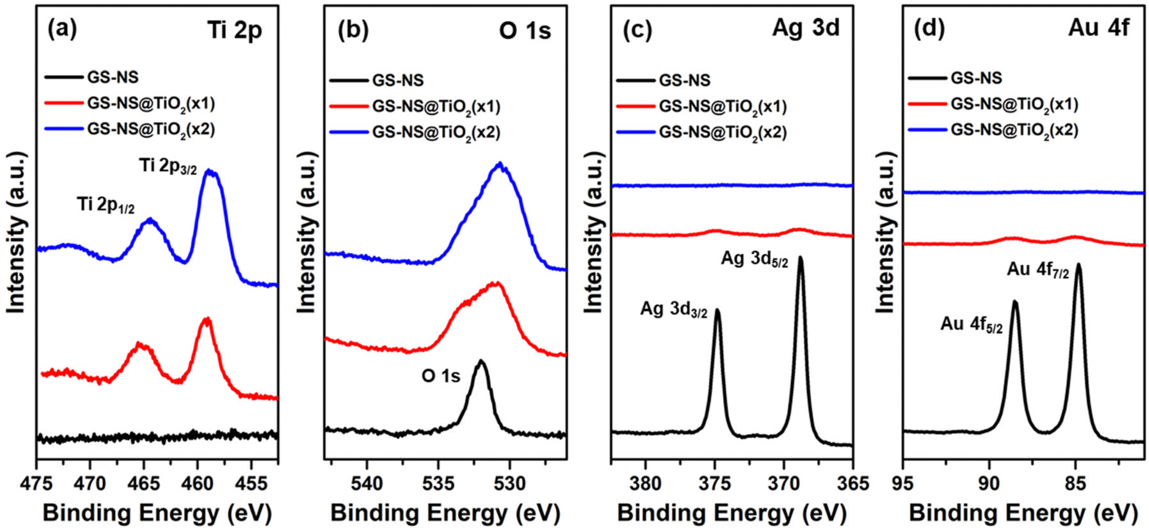

Fig. 6 XPS spectra for (a) Ti 2p region, (b) O 1s region, (c) Ag 3d region, and (d) Au 4f region for the GS–NSs, GS–NS@TiO$_2$(×1), and GS–NS@TiO$_2$(×2) nanoparticles.

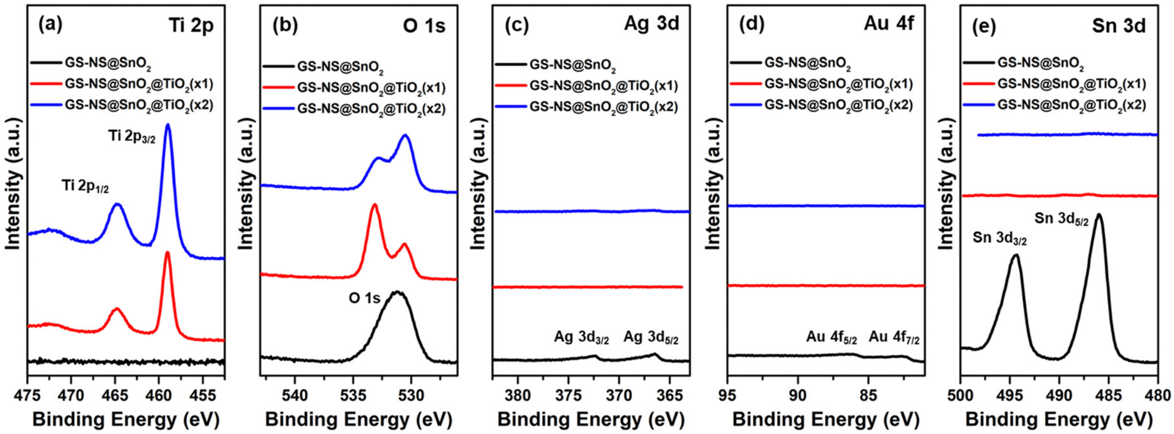

Fig. 7 XPS spectra for the (a) Ti 2p region, (b) O 1s region, (c) Ag 3d region, (d) Au 4f region, and (e) Sn 3d region for the GS–NS@SnO$_2$, GS–NS@SnO$_2$@TiO$_2$(×1), and GS–NS@SnO$_2$@TiO$_2$(×2) nanoparticles.

show the changes in the elemental composition at the surface before and after coating with a TiO$_2$ shell. The relative atomic concentrations of all the elements are presented in Table 2. In general, the XPS intensities and relative compositions show a decrease for the core elements and gradual increase in %Ti with progressive coating steps 1 and 2. In the XPS spectra for pristine GS–NS core nanoparticles (see Fig. 6), no peaks are observed in the Ti 2p region, as expected. The presence of silver is evident from the spectra with sharp peaks for Ag 3d$_{5/2}$ and 3d$_{3/2}$ observed at 368.8 eV and 374.8 eV, respectively.[59] The presence of gold is also evident with sharp peaks for Au 4f$_{7/2}$ and Au 4f$_{5/2}$ clearly observed at 84.8 eV and 88.5 eV, respectively,[60] which confirms the presence of gold and silver originating from the GS–NS. As illustrated by the XPS spectra, after coating with TiO$_2$, peaks corresponding to Ti 2p$_{3/2}$ and 2p$_{1/2}$ at 459.0 eV and 464.3 eV, respectively, appear for both the GS–NS@TiO$_2$(×1) and GS–NS@TiO$_2$(×2) nanoparticles.[59,61] These results further confirm the successful growth of the TiO$_2$ shell on the GS–NS core. A broad peak at 532 eV for oxygen is observed in the O 1s spectra which shows a shift to a lower binding energy with each step of the TiO$_2$ coating.[62] XPS is a surface-specific technique with a penetration depth of about 5–7 nm, and mainly provides the composition at the outer surface of the nanoparticles.[63,64] As observed, the relative concentrations of gold and silver progressively decrease with each coating step, which is evident from the spectra in Fig. 6, where weak intensities are observed in the Ag 3d and Au 4f spectra after one coating but disappear after two rounds of TiO$_2$ coating. These results are consistent with the shell thicknesses calculated from the SEM image analysis, namely, 7 ± 1 nm for GS–NS@TiO$_2$(×1) nanoparticles and 28 ± 11 nm for GS–NS@TiO$_2$(×2) nanoparticles. The relative concentration of Ti appears to change little after the second coating since the first shell itself is almost equivalent to the penetration depth of the XPS technique.

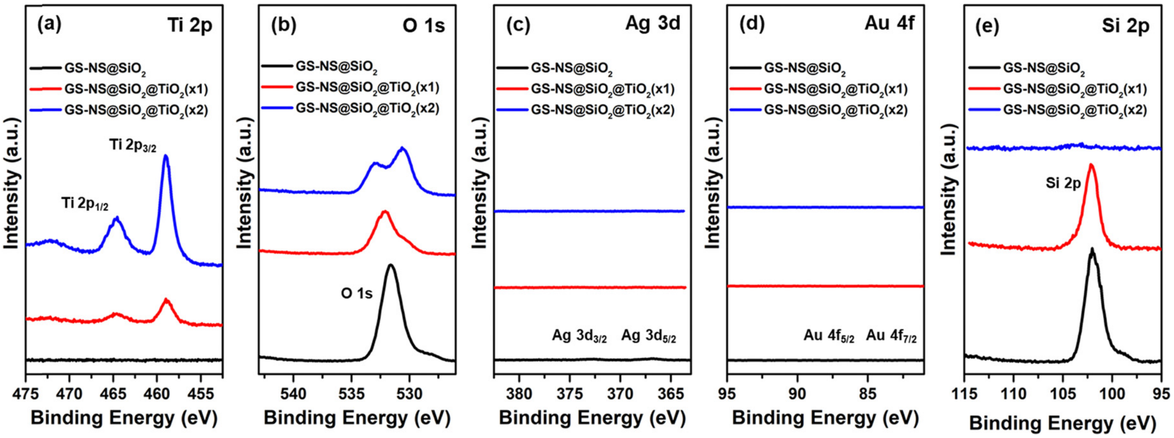

Fig. 8 XPS spectra for the (a) Ti 2p region, (b) O 1s region, (c) Ag 3d region, (d) Au 4f region, and (e) Si 2p region for the GS–NS@SiO_2, GS–NS@SiO_2@TiO_2(×1), and GS–NS@SiO_2@TiO_2(×2) nanoparticles.

Table 2 XPS-derived relative atomic concentrations of Ti, O, Ag, Au, Si, and Sn in the various TiO_2-coated samples

	Relative atomic concentration (%)					
Sample	Ti (2p)	O (1s)	Ag (3d)	Au (4f)	Si (2p)	Sn ($3d_{5/2}$)
GS–NS	0	43	34	19	4	0
GS–NS@TiO_2(×1)	19	75	3	2	1	0
GS–NS@TiO_2(×2)	20	79	0	0	1	0
GS–NS@SnO_2	0	60	2	1	0	38
GS–NS@SnO_2@TiO_2(×1)	12	87	0	0	0	1
GS–NS@SnO_2@TiO_2(×2)	19	78	1	0	1	1
GS–NS@SiO_2	0	67	0	0	31	0
GS–NS@SiO_2@TiO_2(×1)	5	58	0	0	36	0
GS–NS@SiO_2@TiO_2(×2)	19	79	0	0	2	0

Fig. 7 shows the XPS spectra of the particles with a SnO_2 interlayer before and after coating with the TiO_2 shells. After the first round of TiO_2 coating, Ti $2p_{3/2}$ and $2p_{1/2}$ peaks appear in the spectra, and the intensity and relative concentration of Ti 2p increases gradually with each coating step. The peak intensities for Ag 3d and Au 4f are faint because of the SnO_2 shell (11 ± 3 nm). The peaks for Ag and Au, eventually disappear after coating with TiO_2. The peaks for Sn $3d_{5/2}$ and $3d_{3/2}$ at 486.0 eV and 494.5 eV, respectively, can be clearly observed for GS–NS@SnO_2 nanoparticles,[56] becomes negligible after the first round of TiO_2 coating and eventually disappears after the second round of TiO_2 coating. All these observations are in good agreement with thicknesses of the SnO_2 = 11 ± 3 nm, TiO_2(×1) = 4 ± 1 nm, and TiO_2(×2) = 17 ± 4 nm shells in this system. The O 1s spectrum shows a broad peak at around 532 eV for the GS–NS@SnO_2 nanoparticles which becomes broader after one round TiO_2 coating and eventually splits up into two peaks after a second TiO_2 coating. These observations can be attributed to the presence of two different oxides in these nanoparticles.[52] As reported in prior literature, in SnO_2@TiO_2 composites structures, the peak at 532.9 eV corresponds to SnO_2, while the peak at 530.2 eV corresponds to TiO_2.[61,65,66] The intensity of the peak at 532.9 eV, arising from SnO_2, gradually becomes weaker, while the peak at 530.2 eV, arising from TiO_2, becomes stronger with each round of TiO_2 coating. This observation is in good agreement with the above assignment for the two peaks.

In the case of a TiO_2 shell grown on a SiO_2 interlayer, the XPS spectra in Fig. 8 shows that the intensity and relative concentration of the Ti 2p peaks increases gradually with each coating step. The peak intensities for Ag 3d and Au 4f are negligible compared to the GS–NS@SnO_2 nanoparticles because the SiO_2 shell (23 ± 7 nm) is thicker than the SnO_2 shell (11 ± 3 nm). The Si 2p peak remains evident after the first round of TiO_2 coating but eventually disappears after the second round of TiO_2 coating. All these observations further confirm the thicknesses of the SiO_2 = 23 ± 7 nm, TiO_2 (×1) = 5 ± 4 nm, and TiO_2 (×2) = 10 ± 3 nm shells in this system. As observed with SnO_2, the O 1s peak splits up in the presence of both SiO_2 and TiO_2. As reported in prior literature, in structures containing both SiO_2 and TiO_2, the peak at 532.6 eV corresponds to O–Si in SiO_2, while the peak at 530.2 eV corresponds to O–Ti in TiO_2.[52,62,65] The intensity of the peak at 533 eV, corresponding to O–Si gradually becomes weaker, while the peak at 530 eV, corresponding to O–Ti, becomes stronger with each step of the TiO_2 coating, in good agreement with the assignment for the two peaks. As calculated in Table 2, the relative atomic concentrations of Au and Ag are much lower in the XPS measurements, compared to EDX results (Table S1, ESI†), since XPS mainly probes the surface composition, which further confirms that the Au NP and GS–NS cores are consistently covered by TiO_2/SnO_2/SiO_2 shells. Additionally, all the relative atomic concentrations of the TiO_2 coated nanoparticles after the second coating step, are quite similar for all the nanoparticles. Thus, the outer surface of the GS–NS@TiO_2(×2), GS–NS@SiO_2@TiO_2(×2), and GS–NS@SnO_2@TiO_2(×2), comprise almost exclusively of titanium and oxygen confirming complete encapsulation of the GS–NS, GS–NS@SiO_2 and GS–NS@SnO_2 cores with a TiO_2 shell.

3.3. Structural analysis of the nanoparticles

3.3.1. XRD analysis. Powder XRD analysis was conducted to determine the phases present in the nanoparticles. The XRD pattern for the gold–silver nanoshells (and their composite particles) have peaks containing both gold (JCPDS 04-0784)[42,55] and silver (JCPDS 04-0783)[67,68] phases that overlap, confirming an alloyed phase, discussed in detail in our previous paper.[34] For example, the GS–NS@TiO_2 nanoparticles contain FCC cubic phase peaks at 2θ = 38.25°, 44.40°, 64.75°, and 77.65° corresponding to the (111), (200), (220), and (311) crystalline planes, respectively.

After coating the nanoparticles with a TiO_2 shell, XRD analysis was conducted to determine the crystallinity of the shell. The as-synthesized TiO_2-coated nanoparticles do not show any peaks for TiO_2 (as illustrated in Fig. 9). This result indicates that the TiO_2 shell is not crystalline at this stage, consistent with previous studies.[52] The nanoparticles are then annealed at 450 °C for 4 h. The SEM image of GS–NS@SiO_2@TiO_2(×2) in Fig. S3 (ESI†) shows that the discrete morphology is largely retained after the annealing process. XRD analysis of the annealed samples shows additional peaks corresponding to the anatase phase of TiO_2 (JCPDS 21-1272).[69] The peaks at 2θ = 25.38°, 48.05°, 53.95°, 55.04°, 62.85°, and 75.12° correspond to the (101), (200), (105), (211), (204), and (215) planes of anatase TiO_2.[70] The peak at 2θ = 48.05° and the twin peaks at 2θ = 53.95° and 55.04° can be clearly observed; all of which are fingerprint peaks for the anatase phase of TiO_2. Thus, all three types of architectures are amorphous as-synthesized and adopt the anatase phase after annealing. Annealing at 450 °C for 3–4 hours is an established protocol to obtain anatase phase TiO_2.[52] The anatase phase is desirable since the position of the conduction band is ideal to produce hydrogen gas from splitting water.[71] The XRD peak intensities for the anatase phase, albeit weak, are consistent with previous reports for similar morphology and recorded shell thicknesses of the TiO_2 shell synthesized from TBOT.[52] Interestingly, the TiO_2 shell grown on top of a rutile SnO_2 layer adopts the anatase phase as well. Rutile SnO_2 synthesized using the sodium stannate method yields polycrystalline SnO_2 with very small crystallites.[34,56] Hence, the peaks for rutile SnO_2 are not distinctly visible in comparison to peaks arising from the much more crystalline Au–Ag alloy and anatase TiO_2 phases. However, the broad (211) peak characteristic of SnO_2 nanoparticles prepared using this sodium stannate method,[34,56] can be weakly observed at 2θ = 51.51° for the GS–NS@SnO_2@TiO_2(×2) samples. Since SiO_2 is amorphous, no peaks are observed for SiO_2 in the corresponding XRD.[52]

3.4. Optical and electrical properties

3.4.1. UV-Vis spectroscopy. Anatase TiO_2 has an optical band gap of 3.2 eV, which limits its extinction to the UV region only. Previous studies have shown that noble metal nanoparticles typically exhibit strong extinctions in the visible and near-IR region due to localized surface plasmonic resonance.[72,73] Localized surface plasmonic resonance (LSPR) is a unique property exhibited by noble metal nanoparticles and nanoshells where surface electrons couple with the incident light and oscillate at the same frequency, leading to extinctions in the visible region.[73,74] The plasmonic particles chosen for this manuscript are hollow gold–silver nanoshells since they have a tunable and much broader extinction in the visible to near-IR regions compared to Au NPs, enabling better utilization of the solar spectrum by metal oxide materials. As illustrated by the UV-visible spectra in Fig. 10a, GS–NSs were synthesized with LSPRs at ∼500 nm, ∼700 nm,

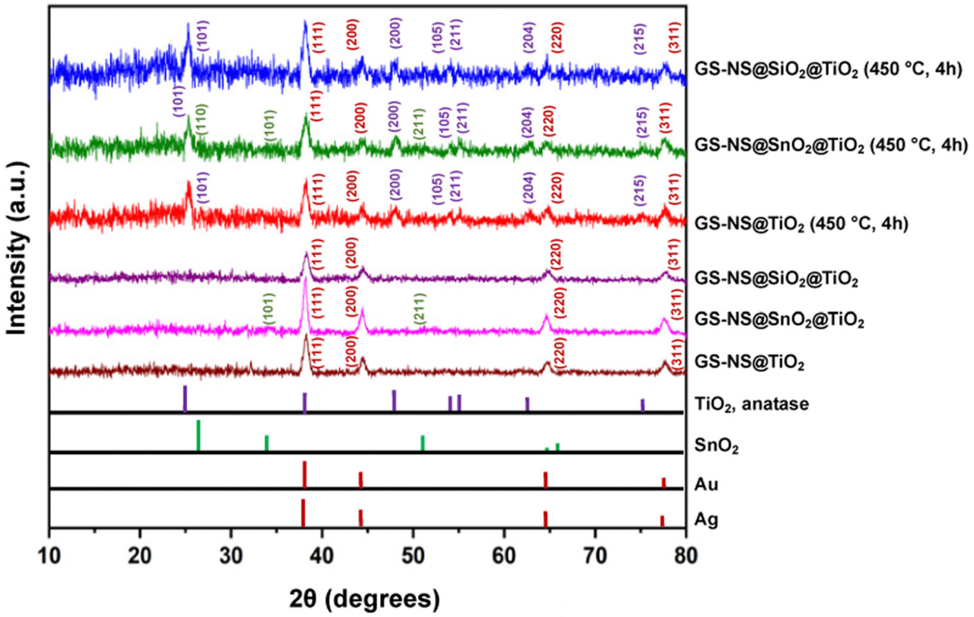

Fig. 9 Powder XRD patterns for GS–NS@TiO_2(×2), GS–NS@SiO_2@TiO_2(×2), and GS–NS@SnO_2@TiO_2(×2) nanoparticles before and after annealing along with their respective reference line patterns.

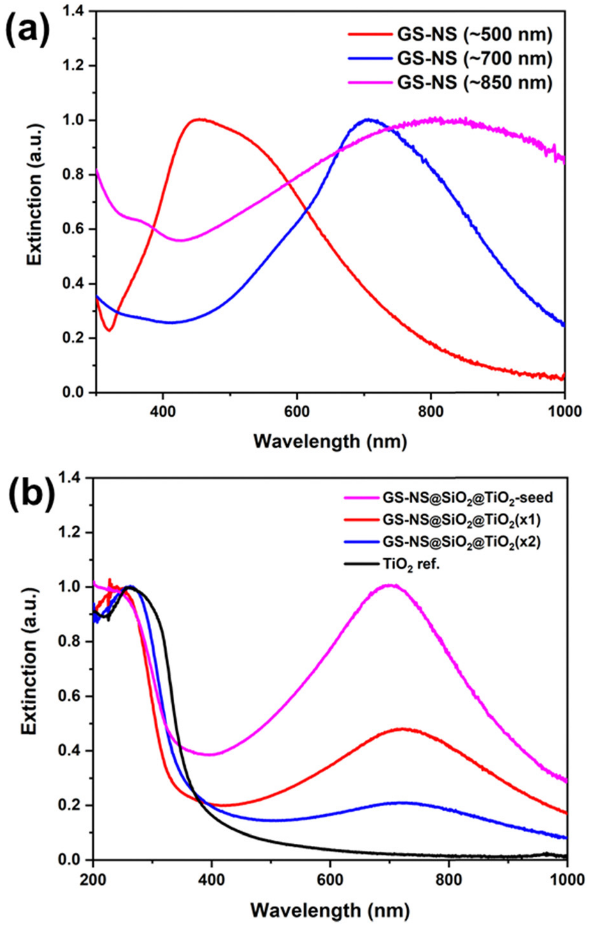

Fig. 10 (a) Extinction spectra of GS–NSs demonstrating tunable LSPR maximum (λ_{max}). Spectra normalized with GS–NS = 1. (b) Extinction spectra of GS–NS@SiO_2 nanoparticles showing relative extinction in visible and UV regions after coating with TiO_2 seeds and TiO_2 shells. Spectra normalized with TiO_2 = 1.

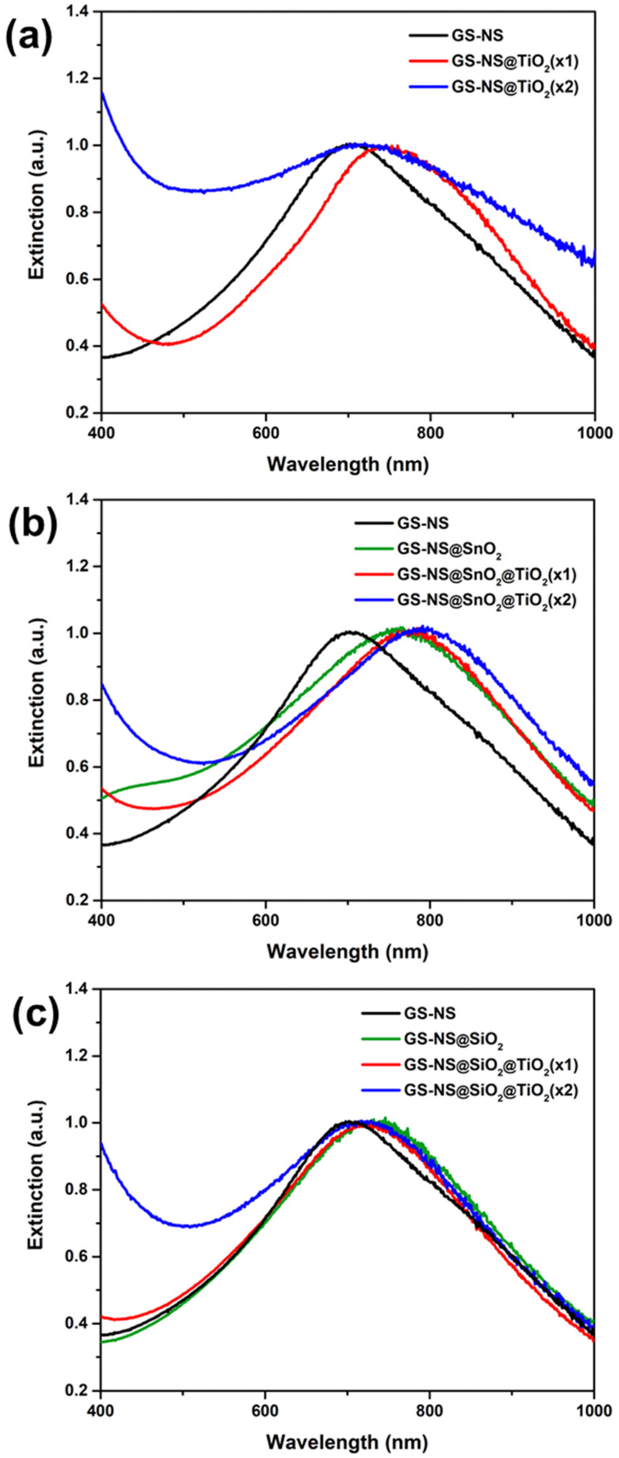

Fig. 11 Extinction spectra in the range of 400–1000 nm for the (a)–(c) GS–NSs, GS–NS@SiO_2, and GS–NS@SnO_2 nanoparticles before and after each round of coating with TiO_2 shells.

and ~850 nm, thereby demonstrating the ability to tune the LSPR extinction maximum of the GS–NSs. In a previous paper, our groups discovered that the incorporation of GS–NSs triggered a strong visible to near-IR extinction in core–shell nanoparticle systems with tin oxide.[34] Theoretical studies of electronic structures (both rutile and anatase) show that TiO_2 has several energetically flat and close-lying levels in the conduction band, while SnO_2 has a single highly dispersive level.[35] Due to this reason, TiO_2 exhibits a much stronger optical extinction than SnO_2 in the UV region. However, as mentioned earlier, both oxides cannot absorb light beyond the UV region on their own. The LSPR properties of GS–NSs can be used to activate visible- and near-IR-light absorption in TiO_2. UV-vis spectroscopy was used to evaluate the optical extinction properties of the nanoparticles. Fig. 11 shows the UV-Vis spectra of the GS–NS nanoparticles (λ_{max} ~ 700 nm) after each coating with SiO_2/SnO_2 and TiO_2 at different steps.

The LSPR peak from the GS–NS core largely retains its plasmonic characteristics after the various stages of coating. The LSPR peak position, however, shows a red-shift after coating with SiO_2/SnO_2 and TiO_2 shells (see Fig. 11a–c). This red-shift is consistent with previous observations of coating plasmonic nanoparticles by materials with higher refractive index (R.I.); notably, the R.I. of SnO_2 (~2.01), SiO_2 (~1.46), and TiO_2 (~2.41) are greater than that of water (~1.33).[75,76] In the case of the GS–NS@TiO_2 nanoparticles, shell thickness after the first and second round of coating are 7 ± 1 nm and 28 ± 11 nm, respectively. Fig. 11a shows a red-shift in the LSPR peak of the GS–NS by about ~40 nm after the first round of coating. After the second round of coating, the position of the LSPR peak is unchanged. Any further red-shift of the peak is masked by broadening as contributions from the extinction tail of the very thick TiO_2 shell increase significantly. In the case of GS–NS@SiO_2@TiO_2 nanoparticles, the thickness of the SiO_2 shell is 23 ± 7 nm, while the thicknesses of the TiO_2 shells after the first and second round of coating are 5 ± 4 nm and 10 ± 3 nm, respectively. Since, the R.I. of SiO_2 is not too different from water, there is a small red-shift of about ~20 nm in the LSPR peak for GS–NS after coating with SiO_2 (see Fig. 11c). After the TiO_2 coating, the position of the LSPR peak remains constant, and no significant red-shift is observed. This phenomenon can perhaps be attributed to the thickness of the SiO_2 shell, which is >20 nm. Hence, further coating with TiO_2 fails to exert a strong influence on the LSPR properties of the inner GS–NS core.

This hypothesis is further proved in the case of the GS–NS@SnO_2@TiO_2 nanoparticles. The thickness of the SnO_2 shell is 11 ± 3 nm, while the thickness of the TiO_2 shell after the first and second round of coating are 4 ± 1 nm and 17 ± 4 nm, respectively. There is an initial red-shift of about ~60 nm in the LSPR peak position for the GS–NS after coating with a SnO_2 shell. Notably, this red-shift is higher than that for just a single shell of SiO_2 since R.I.(SnO_2) > R.I.(SiO_2). Interestingly, this red-shift is also higher than just a single shell of TiO_2 in the GS–NS@TiO_2 nanoparticles, although the R.I.(TiO_2) > R.I.(SnO_2). This phenomenon arises because the thickness of the SnO_2 shell (11 ± 3 nm) is more than the thickness of a single TiO_2 shell (7 ± 1 nm), increasing overall red-shift. In the case of the GS–NS@SnO_2@TiO_2 nanoparticles, Fig. 11b shows a consistent red-shift with every step of TiO_2 coating. Since the thickness of the SnO_2 shell is only 11 ± 3 nm, another red-shift of ~15 nm is observed after the first round of TiO_2 coating. Also, since the first round of TiO_2 coating produces a TiO_2 shell with a thickness of only 4 ± 1 nm, the total combined shell thickness (SnO_2 + TiO_2) is about 15 ± 4 nm, which is still <20 nm; therefore, another red-shift is observed in the LSPR peak position by ~15 nm after the second round of TiO_2 coating. Thus, the LSPR field of the GS–NS is clearly influenced by the TiO_2 coating in each step as long as the combined shell thickness is within ~20 nm. Additionally, as evident from Fig. 11b, since the total TiO_2 shell thickness after both rounds of TiO_2 coatings in GS–NS@SnO_2@TiO_2(×2) is only 17 ± 4 nm thick, hence there is not a strong contribution to the LSPR peak from the extinction tail of TiO_2. Thus, the total red-shift of the LSPR peak alone in the case of GS–NS@SnO_2@TiO_2(×2) nanoparticles is about ~ 90 nm. From these observations, it can be concluded that the LSPR field of hollow GS–NS extends to a range of about ~20 nm. Beyond this range, the LSPR induced field of the GS–NS is not affected as strongly. Thus, the LSPR peak can be red-shifted most effectively by coating them with multiple thin shells (<20 nm) of materials with a high refractive index (≥2.0) rather than a single thick shell.

These observations also indicate that the LSPR induced field of the GS–NS only interacts up to a range of ~20 nm. There have been similar indications of this phenomenon in previous literature as well. For example, Li *et al.* observed that the photocatalytic efficiency of a GS–NS@$ZnIn_2S_4$ photocatalyst was improved when a 17 nm thick SiO_2 interlayer was introduced.[16] However, the sample with an even thicker SiO_2 interlayer of 42 nm thickness performed the worst, even worse than the sample with no interlayer. The range of LSPR field of GS–NS was thus thought to extend up to a maximum of ~40 nm. However, results in this present study provide clear evidence that the LSPR properties of the GS–NS actually extend up to a maximum range of ~20 nm.

Looking at the UV-Vis spectra for the GS–NS@SiO_2@TiO_2 (λ_{max} ~ 700 nm) system as an example (Fig. 10b), one can also evaluate the relative extinctions in visible and UV regions for the various TiO_2 coated systems. As observed, coating TiO_2 introduces a characteristic peak in the UV region corresponding to the excitation of electrons across its band gap. As expected from theoretical predictions, UV extinction by TiO_2 is significantly more intense than the SnO_2-coated nanoparticles.[35] The relative UV extinction due to the TiO_2 band-gap excitation increases rapidly with increasing thickness for all samples. When the amounts of TBOT precursor and water for hydrolysis are increased, thicker shells are obtained, as illustrated by the SEM imaging and size measurements (see Fig. 1–3). With a second round of coating on the TiO_2 coated particles, the thickness increases further, and the UV extinction also increases, as expected. As demonstrated earlier in Fig. 4, the TiO_2 coating recipe can also be modified to synthesize TiO_2-seed decorated nanoparticles. Fig. 10b shows the UV-Vis spectra of TiO_2-seed decorated nanoparticles compared to the ones with complete TiO_2 shells after one and two rounds of coatings. Apparent from the data, relative UV and visible-light extinction intensities in this nanoparticle system can be tuned simply by changing between TiO_2-seeds and TiO_2 shells with various thicknesses. The UV light extinction in the TiO_2-seed decorated nanoparticles is nearly equal to the LSPR extinction in the visible region. These results also hold true for TiO_2-seeding and TiO_2 shells on just GS–NSs and on GS–NS@SnO_2 cores as well. Thus, one can add equivalent levels of UV extinction to plasmonic nanoparticles simply by seeding TiO_2 nanoparticles on its surface, without necessarily coating an entire shell. Overall, using this TiO_2 coating recipe, the relative extinctions in the visible and UV regions can be easily tuned. This feature adds further tunability and versatility to the optical properties of this nanoparticle system.

3.4.2. Photoluminescence spectra and electron/hole recombination. In addition to a lack of extinction beyond the UV region, another major limitation of metal oxide nanoparticles is the recombination of photogenerated electrons and holes.[2,18] The free electrons in the conduction band generated from excitation across the band gap readily recombine with the holes in the valence band instead of participating in the targeted chemical reaction.[18] A few different strategies have been employed to ensure longer separation of these photogenerated electron–hole pairs in semiconductor catalysts.[2,77] Noble metal nanostructures have also been shown to be effective in reducing the rate of electron–hole recombination in various metal oxides.[2,77,78] For metal oxide and noble metal hetero-structured nanoparticle catalysts, the metal oxides are most commonly used as the inner core, and noble metal nanoparticles on the outside either as seeds, partial shells, or complete shells. These hetero-structured nanocomposites have been able to reduce electron–hole recombination in the metal oxide core.[32] Au NPs have been typically used to quench the rate of electron–hole recombination, especially in the case of TiO_2 and SnO_2 photocatalysts.[22,27,78–80] Previous studies conducted by Khantamat *et al.* with gold decorated TiO_2 nanoparticles exhibited effective suppression of electron–hole recombination, leading to higher photocatalytic activity.[79]

In a previous paper,[34] our groups studied a different design with the plasmonic Au NP as the core and the metal oxide as the outer shell. An extremely effective suppression in the rate of electron–hole recombination was observed per particle. When the PL intensities were normalized with respect to the volume of tin oxide material per particle, a nearly complete suppression of the recombination is observed. This result outlined a significant advantage of having the noble metal nanoparticle as the core and the metal oxide as the outer shell. Although Au NPs have been commonly employed for decreasing electron–hole recombination, the use of gold–silver nanoshells was also examined for this purpose. The suppression of electron–hole recombination per volume of tin oxide appears to be more effective with a GS–NS core compared to the ones with an Au NP core, affording a near-complete suppression.

As discussed earlier, TiO_2 absorbs light much more strongly than SnO_2, leading to the creation of a much greater number of electron–hole pairs.[35] This study examines whether the effect of GS–NS core on the electron–hole recombination of TiO_2 also shows similar quenching as observed for SnO_2.[34] To examine the effect of the GS–NS core in quenching the electron–hole recombination in TiO_2, photoluminescence studies were conducted. Photoluminescence intensity in metal oxide semiconductors arises from the energy emitted by the electrons that fall back from the conduction band to recombine with the holes in the valence band. Hence, a drop in the photoluminescence intensity is indicative of a decrease in the rate of electron–hole recombination.[22] Photoluminescence measurements were carried out for all the samples with excitation wavelength at 300 nm to ensure complete band gap excitation in the TiO_2 component. Photoluminescence spectra of the core–shell and core-dual-shell nanoparticles are compared to commercial TiO_2 nanoparticles. For the purpose of meaningful comparison, photoluminescence intensities were normalized with respect to particle concentration and volume of TiO_2 per particle, as shown in Fig. 12. As illustrated in Fig. 12, the GS–NS core effects significant suppression in the rate of electron–hole recombination in TiO_2 as well. This extremely effective quenching of electron–hole recombination in TiO_2 further reiterates the importance of this design where the metal oxide material is employed as the shell with the noble metal core inside. These results prove that the GS–NS core design is effective for the suppression of electron–hole recombination in metal oxides with much higher number of excitons than SnO_2 as well. When the PL intensities are normalized with respect to volume of TiO_2 per particle (see Fig. 12b), the effect of the interlayers becomes more evident in the three different types of TiO_2 core–shell materials synthesized. Among the three types of particles, the recombination is quenched most effectively in the presence of a SnO_2 interlayer, at ∼68%, even better than the particle with no interlayer. The quenching due to the GS–NS core in the

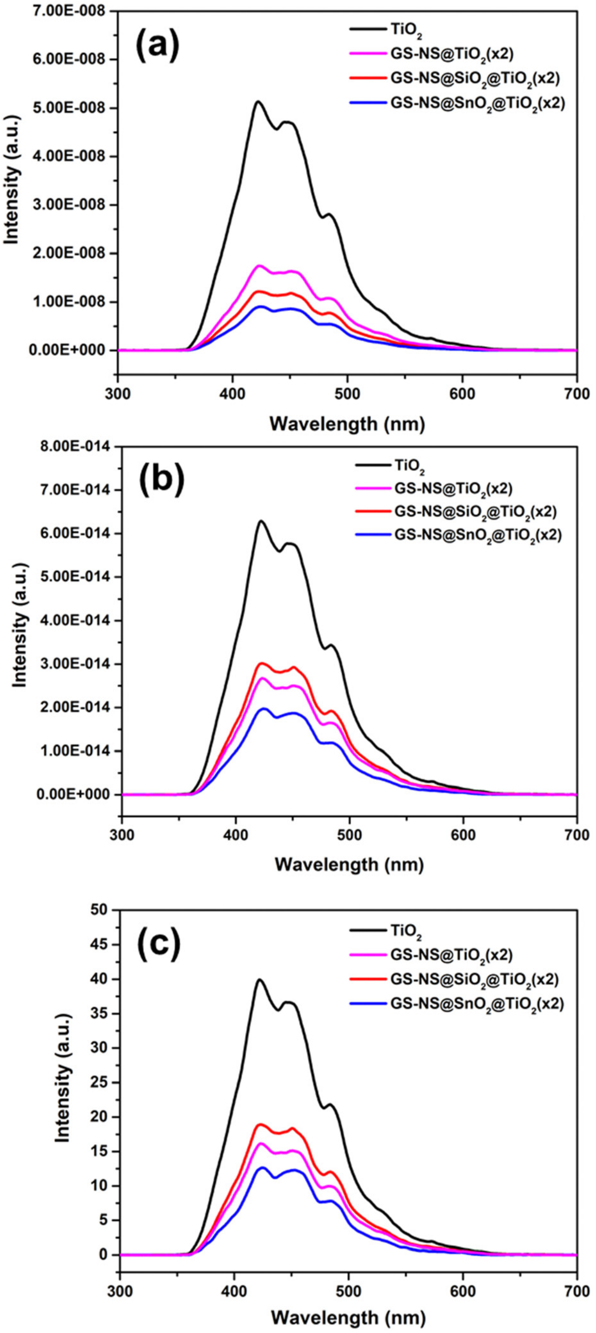

Fig. 12 Photoluminescence spectra of TiO_2, GS–NS@TiO_2(×2), GS–NS@SiO_2@TiO_2(×2), and GS–NS@SnO_2@TiO_2(×2) nanoparticles normalized with respect to (a) particle concentration, (b) particle concentration + volume of TiO_2 per particle, and (c) TiO_2 extinction intensity.

GS–NS@TiO_2 was found to be ∼56%, while for the GS–NS@SiO_2@TiO_2 nanoparticles, the quenching was the lowest at ∼49%. However, these results suggest that even in the presence of an insulating SiO_2 interlayer between the GS–NS and TiO_2, the GS–NS can still accept electrons from the TiO_2 shell and increase the lifetime of charge carriers. This phenomenon can plausibly be attributed to tunneling due to the mesoporous nature of the SiO_2 shell, or to the presence of small TiO_2 particulates within the SiO_2 interlayer, facilitating electron transfer to the GS–NS core.

To verify these trends, the photoluminescence spectra were normalized with respect to the intensity of UV extinction due to TiO_2 in the corresponding samples (see Fig. 12c). As expected, the trends in Fig. 12c closely correlate those in Fig. 12b, confirming the effect of the interlayers on the charge transfer and recombination characteristics. The quenching in GS–NS@TiO_2, GS–NS@SnO_2@TiO_2, and GS–NS@SiO_2@TiO_2 nanoparticles was calculated to be ∼58%, ∼68%, and 50%, respectively, when normalized with TiO_2 extinction intensity. These results together confirm that electron–hole recombination of TiO_2 is most effectively suppressed in the presence of a SnO_2 interlayer, which can likely be attributed to the type-II heterojunction characteristics between the SnO_2 interlayer and the TiO_2 shell. In addition to charge-carrier trapping by the GS–NS core, additional electrons can be trapped in the conduction band of SnO_2, increasing their lifetime. As reported in previous studies, electrons move from the CB of TiO_2 to the CB of SnO_2, while the holes from VB of SnO_2 move in the opposite direction towards VB of TiO_2 in such a system.[46,48] This orchestration allows for highly effective separation of charge carriers.[48] Given the polycrystalline porous nature of both the TiO_2 and SnO_2 shells,[34,36,52,58] all parts of the nanoparticle are accessible; chemical species in solution can easily access any part of the nanoparticle to react with either holes or electrons.

In a previous paper, our groups had also demonstrated the ability to modify the GS–NS@SnO_2 recipe to generate doped tin oxide shells with antimony and zinc,[34] which was achieved simply by adding sodium antimonate and sodium zincate to sodium stannate in the tin oxide coating step. When combined with the ability to alter the band gap and conductivity of the tin oxide interlayer material by doping with antimony and zinc, this recipe allows us to design finely tailored heterojunctions with TiO_2 while keeping the chemistry consistent, which will greatly enhance our ability to modulate electronic structures on the nanoscale.

4. Conclusions

We successfully demonstrated a strategy to compensate for the drawbacks and enhance the utility of TiO_2. A single facile and versatile solution was developed for the controlled growth of TiO_2 shells directly on a noble metal core consisting of GS–NSs, as well as on GS–NSs with a semiconducting (SnO_2) and insulating (SiO_2) interlayer. The versatility of both this method and optimization approach allows us to utilize a single synthesis procedure to coat uniform TiO_2 shells on multiple diverse cores, such as a crystalline metal, polycrystalline metal oxide, and amorphous silica. Measurements of the optical properties showed that the plasmonic core–shell and core-dual-shell nanoparticles exhibit strong extinctions in the visible and near-IR regions, respectively, and that the position of extinction maximum (λ_{max}) can be successfully tuned within this region. This strong LSPR extinction can extend the utility of TiO_2 well beyond the UV region. Further, the relative extinctions in the UV, visible, and near-IR regions can be carefully tailored by changing the ratio of Au/Ag in the GS–NS alloy and/or by controlled TiO_2 coating/seeding methods reported herein. The range of the LSPR field for the GS–NSs was also thoroughly investigated and found to extend up to ∼20 nm. Incorporation of the GS–NS core also demonstrated a remarkable suppression in the rate of electron–hole recombination in TiO_2. This observation further establishes the utility of plasmonic gold–silver nanoshells and paves the way for their use in enhancing the properties of other traditional semiconductor materials as well. Importantly, this exceptional reduction of the electron–hole recombination further demonstrates the effectiveness of designing the plasmonic nanoparticle as the core and the metal oxide as the shell.

This synthesis method is easily transferable to generate TiO_2 shells on GS–NS with a semiconducting SnO_2 interlayer or an insulating SiO_2 interlayer. Moreover, by virtue of the facile and consistent synthetic method described herein, SnO_2 shells now offer a viable semiconductor alternative to traditional silica shells. Like SiO_2, the SnO_2 shell can also be easily functionalized using recipes used for SiO_2, while possessing multiple advantages such as having a tunable semiconducting band gap[34,56] and stability across a wider pH range.[58] The results demonstrate that the presence of different interlayers between the GS–NS and TiO_2 shell can change the localized plasmonic effects, energy-transfer, charge-transfer, and recombination properties in these systems. The extinction spectra of the three different types of nanoparticles demonstrate that the LSPR field of GS–NS extend to a range of 20 nm, and can be red-shifted most effectively with successive addition of thin interlayers (<5 nm each) with a high refractive index (>2.0) instead of a single thick layer. The nanoparticles with an SnO_2 interlayer also afforded the greatest suppression of TiO_2 recombination. The successful synthesis of visible/near-IR-active SnO_2/TiO_2 composite nanoparticles with proposed type-II heterojunction characteristics opens the door for novel optoelectronic possibilities. Combined with the ability to vary the SiO_2 shell thickness[81] and modulate the band gap of SnO_2 *via* doping,[34,56] this versatile TiO_2 coating method affords us multiple handles to tune the electrical properties in nanoscale colloids. This work provides a good foundation for the synthesis of core-dual-shell tunable-heterojunction nanoparticles, which can be further developed in terms of the shell smoothness by employing templated methods such as using block copolymers as nanoreactors, which has been reported previously.[82–86] On the whole, a combination of these optical and electrical properties should render these unique hybrid particles effective materials for photovoltaics, photocatalysis, optoelectronic devices, and sensors.

Author contributions

Riddhiman Medhi: conceptualization, investigation, methodology, data curation, formal analysis, visualization, writing – original draft. Sarawut Plengjaroensirichai: investigation, methodology. Nhat Ngo: investigation, methodology. Maria D. Marquez: supervision, validation, project administration, writing – review & editing. Pannaree Srinoi: investigation, methodology. Hung-Vu Tran: project administration. Allan J. Jacobson: conceptualization, supervision. Tai-Chou Lee: conceptualization, funding acquisition. T. Randall Lee: funding acquisition, project administration, conceptualization, supervision, validation, formal analysis, resources, writing – review and editing.

Data availability

Data will be made available on request.

Conflicts of interest

The authors declare that they have no known competing financial interests or personal relationships that could have appeared to influence the work reported in this paper.

Acknowledgements

We thank the Air Force Office of Scientific Research (FA9550-20-1-0349; 20RT0302 and FA9550-23-1-0581; 23RT0567) and the Robert A. Welch Foundation (Grant No. E-1320 and E-0024) for generously supporting this research. The authors would also like to thank Zhenglin Zhang for aiding with the PL measurements.

References

1 A. Dey, Semiconductor Metal Oxide Gas Sensors: A Review, *Mater. Sci. Eng., B*, 2018, **229**, 206–217.

2 C. Ray and T. Pal, Recent Advances of Metal–Metal Oxide Nanocomposites and their Tailored Nanostructures in Numerous Catalytic Applications, *J. Mater. Chem. A*, 2017, **5**, 9465–9487.

3 X. Yu, T. J. Marks and A. Facchetti, Metal Oxides for Optoelectronic Applications, *Nat. Mater.*, 2016, **15**, 383.

4 Y. Liu, W. Wang, X. Xu, J.-P. Marcel Veder and Z. Shao, Recent Advances in Anion-Doped Metal Oxides for Catalytic Applications, *J. Mater. Chem. A*, 2019, **7**, 7280–7300.

5 A. Raghunath and E. Perumal, Metal Oxide Nanoparticles as Antimicrobial Agents: A Promise for the Future, *Int. J. Antimicrob. Agents*, 2017, **49**, 137–152.

6 R. Daghrir, P. Drogui and D. Robert, Modified TiO_2 For Environmental Photocatalytic Applications: A Review, *Ind. Eng. Chem. Res.*, 2013, **52**, 3581–3599.

7 R. Medhi, M. D. Marquez and T. R. Lee, Visible-Light-Active Doped Metal Oxide Nanoparticles: Review of their Synthesis, Properties, and Applications, *ACS Appl. Nano Mater.*, 2020, **3**, 6156–6185.

8 Y.-T. Chen, R. Medhi, I. Nekrashevich, D. Litvinov, S. Xu and T. R. Lee, Specific Detection of Proteins Using Exceptionally Responsive Magnetic Particles, *Anal. Chem.*, 2018, **90**, 6749–6756.

9 R. Medhi, P. Srinoi, N. Ngo, H.-V. Tran and T. R. Lee, Nanoparticle-Based Strategies to Combat COVID-19, *ACS Appl. Nano Mater.*, 2020, **3**, 8557–8580.

10 B. Zeng, S. Wang, Y. Xiao, G. Zeng, X. Zhang, R. Li and C. Li, Surface Phosphate Functionalization for Boosting Plasmon-Induced Water Oxidation on Au/TiO_2, *J. Phys. Chem. C*, 2022, **126**, 5167–5174.

11 D. J. Da Silva, A. G. Souza, G. D. S. Ferreira, A. Duran, A. D. Cabral, F. L. A. Fonseca, R. F. Bueno and D. S. Rosa, Cotton Fabrics Decorated with Antimicrobial Ag-Coated TiO_2 Nanoparticles Are Unable to Fully and Rapidly Eradicate SARS-CoV-2, *ACS Appl. Nano Mater.*, 2021, **4**, 12949–12956.

12 A. Jaroenworaluck, W. Sunsaneeyametha, N. Kosachan and R. Stevens, Characteristics of Silica-Coated TiO_2 and its UV Absorption for Sunscreen Cosmetic Applications, *Surf. Interface Anal.*, 2006, **38**, 473–477.

13 C. M. Staller, Z. L. Robinson, A. Agrawal, S. L. Gibbs, B. L. Greenberg, S. D. Lounis, U. R. Kortshagen and D. J. Milliron, Tuning Nanocrystal Surface Depletion by Controlling Dopant Distribution as a Route Toward Enhanced Film Conductivity, *Nano Lett.*, 2018, **18**, 2870–2878.

14 K. M. Noone and D. S. Ginger, Doping for Speed: Colloidal Nanoparticles for Thin-Film Optoelectronics, *ACS Nano*, 2009, **3**, 261–265.

15 S. E. Lohse and C. J. Murphy, Applications of Colloidal Inorganic Nanoparticles: From Medicine to Energy, *J. Am. Chem. Soc.*, 2012, **134**, 15607–15620.

16 C.-H. Li, M.-C. Li, S.-P. Liu, A. C. Jamison, D. Lee, T. R. Lee and T.-C. Lee, Plasmonically Enhanced Photocatalytic Hydrogen Production from Water: The Critical Role of Tunable Surface Plasmon Resonance from Gold–Silver Nanoshells, *ACS Appl. Mater. Interfaces*, 2016, **8**, 9152–9161.

17 P. Mazierski, A. Mikolajczyk, B. Bajorowicz, A. Malankowska, A. Zaleska-Medynska and J. Nadolna, The Role of Lanthanides in TiO_2-Based Photocatalysis: A Review, *Appl. Catal., B*, 2018, **233**, 301–317.

18 B. Ohtani, Titania Photocatalysis beyond Recombination: A Critical Review, *Catalysts*, 2013, **3**, 942–953.

19 P. Wang, B. Huang, Y. Dai and M.-H. Whangbo, Plasmonic Photocatalysts: Harvesting Visible Light with Noble Metal Nanoparticles, *Phys. Chem. Chem. Phys.*, 2012, **14**, 9813–9825.

20 E. Petryayeva and U. J. Krull, Localized Surface Plasmon Resonance: Nanostructures, Bioassays and Biosensing—A Review, *Anal. Chim. Acta*, 2011, **706**, 8–24.

21 W. W. Brian, R. Medhi, M. D. Marquez, S. Rittikulsittichai, M. Tran and T. R. Lee, Porous Silver-Coated pNIPAM-*co*-AAc Hydrogel Nanocapsules, *Beilstein J. Nanotechnol.*, 2019, **10**, 1973–1982.

22 M. M. Khan, S. A. Ansari, M. E. Khan, M. O. Ansari, B.-K. Min and M. H. Cho, Visible Light-Induced Enhanced

Photoelectrochemical and Photocatalytic Studies of Gold Decorated SnO_2 Nanostructures, *New J. Chem.*, 2015, **39**, 2758–2766.

23 V. Vongsavat, B. M. Vittur, W. W. Bryan, J.-H. Kim and T. R. Lee, Ultrasmall Hollow Gold–Silver Nanoshells with Extinctions Strongly Red-Shifted to the Near-Infrared, *ACS Appl. Mater. Interfaces*, 2011, **3**, 3616–3624.

24 C. Zhang, Y. Zhou, A. Merg, C. Song, G. C. Schatz and N. L. Rosi, Hollow Spherical Gold Nanoparticle Superstructures with Tunable Diameters and Visible to Near-Infrared Extinction, *Nanoscale*, 2014, **6**, 12328–12332.

25 L. Zhang, K. Xia, Z. Lu, G. Li, J. Chen, Y. Deng, S. Li, F. Zhou and N. He, Efficient and Facile Synthesis of Gold Nanorods with Finely Tunable Plasmonic Peaks from Visible to Near-IR Range, *Chem. Mater.*, 2014, **26**, 1794–1798.

26 I. G. Theodorou, Z. A. R. Jawad, Q. Jiang, E. O. Aboagye, A. E. Porter, M. P. Ryan and F. Xie, Gold Nanostar Substrates for Metal-Enhanced Fluorescence through the First and Second Near-Infrared Windows, *Chem. Mater.*, 2017, **29**, 6916–6926.

27 T.-M. Chen, G.-Y. Xu, H. Ren, H. Zhang, Z.-Q. Tian and J.-F. Li, Synthesis of Au@TiO_2 Core–Shell Nanoparticles with Tunable Structures for Plasmon-Enhanced Photocatalysis, *Nanoscale Adv.*, 2019, **1**, 4522–4528.

28 J. Goebl, J. B. Joo, M. Dahl and Y. Yin, Synthesis of Tailored Au@TiO_2 Core–Shell Nanoparticles for Photocatalytic Reforming of Ethanol, *Catal. Today*, 2014, **225**, 90–95.

29 X.-F. Wu, H.-Y. Song, J.-M. Yoon, Y.-T. Yu and Y.-F. Chen, Synthesis of Core–Shell Au@TiO_2 Nanoparticles with Truncated Wedge-Shaped Morphology and Their Photocatalytic Properties, *Langmuir*, 2009, **25**, 6438–6447.

30 W.-L. Liu, F.-C. Lin, Y.-C. Yang, C.-H. Huang, S. Gwo, M. H. Huang and J.-S. Huang, The Influence of Shell Thickness of Au@TiO_2 Core–Shell Nanoparticles on the Plasmonic Enhancement Effect in Dye-Sensitized Solar Cells, *Nanoscale*, 2013, **5**, 7953–7962.

31 R. Wang, J. Zhang, Y. Zhu, Z. Chai, Z. An, X. Shu, H. Song, X. Xiang and J. He, Selective Photocatalytic Activation of Ethanol C–H and O–H Bonds over Multi-Au@SiO_2/TiO_2: Role of Catalyst Surface Structure and Reaction Kinetics, *ACS Appl. Mater. Interfaces*, 2022, **14**, 2848–2859.

32 J. Xue, L. Wu, C. Deng, D. Tang, S. Wang, H. Ji, C. Chen, Y. Zhang and J. Zhao, Plasmon-Mediated Electrochemical Activation of Au/TiO_2 Nanostructure-Based Photoanodes for Enhancing Water Oxidation and Antibiotic Degradation, *ACS Appl. Nano Mater.*, 2022, **5**, 11342–11351.

33 H. Wu, P. Wang, H. He and Y. Jin, Controlled Synthesis of Porous Ag/Au Bimetallic Hollow Nanoshells with Tunable Pasmonic and Catalytic Properties, *Nano Res.*, 2012, **5**, 135–144.

34 R. Medhi, C.-H. Li, S. H. Lee, P. Srinoi, M. D. Marquez, F. Robles-Hernandez, A. J. Jacobson, T.-C. Lee and T. R. Lee, Antimony- and Zinc-Doped Tin Oxide Shells Coated on Gold Nanoparticles and Gold–Silver Nanoshells Having Tunable Extinctions for Sensing and Photonic Applications, *ACS Appl. Nano Mater.*, 2020, **3**, 8958–8971.

35 M. Dou and C. Persson, Comparative Study of Rutile and Anatase SnO_2 and TiO_2: Band-Edge Structures, Dielectric Functions, and Polaron Effects, *J. Appl. Phys.*, 2013, **113**, 083703.

36 R. Medhi, N. Ngo, T.-C. Lee and T. R. Lee, Type-II Heterojunctions in SnO_2-Coated TiO_2 Core–Shell Nanoparticles, *Curr. Res. Mater. Sci.*, 2021, **3**, 112.

37 G. Yang, Z. Jiang, H. Shi, T. Xiao and Z. Yan, Preparation of Highly Visible-Light Active N-Doped TiO_2 Photocatalyst, *J. Mater. Chem.*, 2010, **20**, 5301–5309.

38 J. Shao, W. Sheng, M. Wang, S. Li, J. Chen, Y. Zhang and S. Cao, In Situ Synthesis of Carbon-Doped TiO_2 Single-Crystal Nanorods with a Remarkably Photocatalytic Efficiency, *Appl. Catal., B*, 2017, **209**, 311–319.

39 R. Jaiswal, J. Bharambe, N. Patel, A. Dashora, D. C. Kothari and A. Miotello, Copper and Nitrogen Co-Doped TiO_2 Photocatalyst with Enhanced Optical Absorption and Catalytic Activity, *Appl. Catal., B*, 2015, **168–169**, 333–341.

40 A. Eshaghi and H. Moradi, Optical and Photocatalytic Properties of the Fe-Doped TiO_2 Nanoparticles Loaded on the Activated Carbon. *Adv*, *Powder Technol.*, 2018, **29**, 1879–1885.

41 S. P. Takle, S. D. Naik, S. K. Khore, S. A. Ohwal, N. M. Bhujbal, S. L. Landge, B. B. Kale and R. S. Sonawane, Photodegradation of Spent Wash, A Sugar Industry Waste, using Vanadium-Doped TiO_2 Nanoparticles, *RSC Adv.*, 2018, **8**, 20394–20405.

42 S. H. Lee, D. M. Hoffman, A. J. Jacobson and T. R. Lee, Transparent, Homogeneous Tin Oxide (SnO_2) Thin Films Containing SnO_2-Coated Gold Nanoparticles, *Chem. Mater.*, 2013, **25**, 4697–4702.

43 N. G. Bastús, F. Merkoçi, J. Piella and V. Puntes, Synthesis of Highly Monodisperse Citrate-Stabilized Silver Nanoparticles of up to 200 nm: Kinetic Control and Catalytic Properties, *Chem. Mater.*, 2014, **26**, 2836–2846.

44 P. Yuan, R. Ma, N. Gao, M. Garai and Q.-H. Xu, Plasmon Coupling-Enhanced Two-Photon Photoluminescence of Au@Ag Core–Shell Nanoparticles and Applications in the Nuclease Assay, *Nanoscale*, 2015, **7**, 10233–10239.

45 A. M. Brito-Silva, R. G. Sobral-Filho, R. Barbosa-Silva, C. B. de Araújo, A. Galembeck and A. G. Brolo, Improved Synthesis of Gold and Silver Nanoshells, *Langmuir*, 2013, **29**, 4366–4372.

46 C. Wang, C. Shao, X. Zhang and Y. Liu, SnO_2 Nanostructures-TiO_2 Nanofibers Heterostructures: Controlled Fabrication and High Photocatalytic Properties, *Inorg. Chem.*, 2009, **48**, 7261–7268.

47 M. K. Gish, A. M. Lapides, M. K. Brennaman, J. L. Templeton, T. J. Meyer and J. M. Papanikolas, Ultrafast Recombination Dynamics in Dye-Sensitized SnO_2/TiO_2 Core/Shell Films, *J. Phys. Chem. Lett.*, 2016, **7**, 5297–5301.

48 X. Huang, L. Shang, S. Chen, J. Xia, X. Qi, X. Wang, T. Zhang and X.-M. Meng, Type-II ZnO Nanorod–SnO_2 Nanoparticle Heterostructures: Characterization of Structural, Optical and Photocatalytic Properties, *Nanoscale*, 2013, **5**, 3828–3833.

49 N. S. McCool, J. R. Swierk, C. T. Nemes, C. A. Schmuttenmaer and T. E. Mallouk, Dynamics of Electron Injection in SnO_2/TiO_2 Core/Shell Electrodes for Water-Splitting Dye-Sensitized Photoelectrochemical Cells, *J. Phys. Chem. Lett.*, 2016, **7**, 2930–2934.

50 L. Troian-Gautier, R. N. Sampaio, E. J. Piechota, M. D. Brady and G. J. Meyer, Barriers for Interfacial Back-Electron Transfer: A Comparison between TiO_2 and SnO_2/TiO_2 Core/Shell Structures, *J. Chem. Phys.*, 2018, **150**, 041719.

51 K. Vinodgopal, I. Bedja and P. V. Kamat, Nanostructured Semiconductor Films for Photocatalysis. Photoelectrochemical Behavior of SnO_2/TiO_2 Composite Systems and Its Role in Photocatalytic Degradation of a Textile Azo Dye, *Chem. Mater.*, 1996, **8**, 2180–2187.

52 J.-W. Lee, S. Kong, W.-S. Kim and J. Kim, Preparation and Characterization of SiO_2/TiO_2 Core–Shell Particles with Controlled Shell Thickness, *Mater. Chem. Phys.*, 2007, **106**, 39–44.

53 J. W. Lee, K. Hong, W. S. Kim and J. Kim, Effect of HPC Concentration and Ultrasonic Dispersion on the Morphology of Titania-Coated Silica Particles, *J. Ind. Eng. Chem.*, 2005, **11**, 609–614.

54 Z. W. Seh, S. Liu, S.-Y. Zhang, K. W. Shah and M.-Y. Han, Synthesis and Multiple Reuse of Eccentric Au@TiO_2 Nanostructures as Catalysts, *Chem. Commun.*, 2011, **47**, 6689–6691.

55 H.-M. Song, B.-S. Chon, S.-H. Jeon, P. Rai, Y.-T. Yu and P. K. Dutta, Synthesis of Au@SnO_2 Core–Shell Nanoparticles with Controllable Shell Thickness and their CO Sensing Properties, *Mater. Chem. Phys.*, 2015, **166**, 87–94.

56 R. Medhi, C.-H. Li, S. H. Lee, M. D. Marquez, A. J. Jacobson, T.-C. Lee and T. R. Lee, Uniformly Spherical and Monodisperse Antimony- and Zinc-Doped Tin Oxide Nanoparticles for Optical and Electronic Applications, *ACS Appl. Nano Mater.*, 2019, **2**, 6554–6564.

57 Q. Chen, Y. Ge, H. Granbohm and S.-P. Hannula, Effect of Ethanol on Ag@Mesoporous Silica Formation by In Situ Modified Stöber Method, *Nanomaterials*, 2018, **8**, 362.

58 S. H. Lee, I. Rusakova, D. M. Hoffman, A. J. Jacobson and T. R. Lee, Monodisperse SnO_2-Coated Gold Nanoparticles Are Markedly More Stable than Analogous SiO_2-Coated Gold Nanoparticles, *ACS Appl. Mater. Interfaces*, 2013, **5**, 2479–2484.

59 J. Sheng, H. Tong, H. Xu and C. Tang, Preparation and Photocatalytic Activity of SnO_2@TiO_2 Core–Shell Composites Modified by Ag, *Catal. Surv. Asia*, 2016, **20**, 167–172.

60 D. P. Anderson, R. H. Adnan, J. F. Alvino, O. Shipper, B. Donoeva, J.-Y. Ruzicka, H. Al Qahtani, H. H. Harris, B. Cowie, J. B. Aitken, V. B. Golovko, G. F. Metha and G. G. Andersson, Chemically Synthesised Atomically Precise Gold Clusters Deposited and Activated on Titania. Part II, *Phys. Chem. Chem. Phys.*, 2013, **15**, 14806–14813.

61 A. Kumar, L. Rout, L. S. K. Achary, A. Mohanty, R. S. Dhaka and P. Dash, An Investigation into the Solar Light-Driven Enhanced Photocatalytic Properties of a Graphene Oxide–SnO_2–TiO_2 Ternary Nanocomposite, *RSC Adv.*, 2016, **6**, 32074–32088.

62 M. Andrulevičius, S. Tamulevičius, Y. Gnatyuk, N. Vityuk, N. Smirnova and A. Eremenko, XPS Investigation of $TiO_2/ZrO_2/SiO_2$ Films Modified with Ag/Au Nanoparticles, *Mater. Sci. Medzg*, 2008, **14**, 8–14.

63 Z. Yang, X. Lu, W. Tan, J. Zhao, D. Yang, Y. Yang, Y. He and K. Zhou, XPS Studies of Nitrogen Doping Niobium used for Accelerator Applications, *Appl. Surf. Sci.*, 2018, **439**, 1119–1126.

64 J. B. Gilbert, M. F. Rubner and R. E. Cohen, Depth-Profiling X-Ray Photoelectron Spectroscopy (XPS) Analysis of Interlayer Diffusion in Polyelectrolyte Multilayers, *Proc. Natl. Acad. Sci. U. S. A.*, 2013, **110**, 6651.

65 G. M. Ingo, S. Dirè and F. Babonneau, XPS Studies of SiO_2–TiO_2 Powders Prepared by Sol-Gel Process, *Appl. Surf. Sci.*, 1993, **70–71**, 230–234.

66 Z. Zhang, Y. Ma, X. Bu, Q. Wu, Z. Hang, Z. Dong and X. Wu, Facile One-Step Synthesis of TiO_2/Ag/SnO_2 Ternary Heterostructures with Enhanced Visible Light Photocatalytic Activity, *Sci. Rep.*, 2018, **8**, 10532.

67 A. Shahzad, W.-S. Kim and T. Yu, A Facile Synthesis of Ag/AgCl Hybrid Nanostructures with Tunable Morphologies and Compositions as Advanced Visible Light Plasmonic Photocatalysts, *Dalton Trans.*, 2016, **45**, 9158–9165.

68 J. Helmlinger, M. Heise, M. Heggen, M. Ruck and M. Epple, A Rapid, High-Yield and Large-Scale Synthesis of Uniform Spherical Silver Nanoparticles by a Microwave-Assisted Polyol Process, *RSC Adv.*, 2015, **5**, 92144–92150.

69 D. Zhang, F. Jing, F. Gao, L. Shen, D. Sun, J. Zhou, Y. Chen and S. Ruan, Enhanced Performance of a TiO_2 Ultraviolet Detector Modified with Graphene Oxide, *RSC Adv.*, 2015, **5**, 83795–83800.

70 H. Zhu, J. Tao and X. Dong, Preparation and Photoelectrochemical Activity of Cr-Doped TiO_2 Nanorods with Nanocavities, *J. Phys. Chem. C*, 2010, **114**, 2873–2879.

71 A. Ganguly, O. Anjaneyulu, K. Ojha and A. K. Ganguli, Oxide-Based Nanostructures for Photocatalytic and Electrocatalytic Applications, *CrystEngComm*, 2015, **17**, 8978–9001.

72 C.-H. Li, A. C. Jamison, S. Rittikulsittichai, T.-C. Lee and T. R. Lee, In Situ Growth of Hollow Gold–Silver Nanoshells within Porous Silica Offers Tunable Plasmonic Extinctions and Enhanced Colloidal Stability, *ACS Appl. Mater. Interfaces*, 2014, **6**, 19943–19950.

73 S. W. Verbruggen, M. Keulemans, J. A. Martens and S. Lenaerts, Predicting the Surface Plasmon Resonance Wavelength of Gold–Silver Alloy Nanoparticles, *J. Phys. Chem. C*, 2013, **117**, 19142–19145.

74 R. G. Navarro Julien and F. Lerouge, From Gold Nanoparticles to Luminescent Nano-Objects: Experimental Aspects for Better Gold-Chromophore Interactions, *Nanophotonics*, 2017, **6**, 71–92.

75 G. Oldfield, T. Ung and P. Mulvaney, Au@SnO_2 Core–Shell Nanocapacitors, *Adv. Mater.*, 2000, **12**, 1519–1522.

76 L. M. Liz-Marzán, M. Giersig and P. Mulvaney, Synthesis of Nanosized Gold−Silica Core−Shell Particles, *Langmuir*, 1996, **12**, 4329–4335.

77 P. Riente and T. Noël, Application of Metal Oxide Semiconductors in Light-Driven Organic Transformations, *Catal. Sci. Technol.*, 2019, **9**, 5186–5232.

78 E. Fudo, A. Tanaka and H. Kominami, AuOx Surface Oxide Layer as a Hole-Transferring Cocatalyst for Water Oxidation over Au Nanoparticle-Decorated TiO_2 Photocatalysts, *ACS Appl. Nano Mater.*, 2022, **5**, 8982–8990.

79 O. Khantamat, C.-H. Li, S.-P. Liu, T. Liu, H. J. Lee, O. Zenasni, T.-C. Lee, C. Cai and T. R. Lee, Broadening the Photoresponsive Activity of Anatase Titanium Dioxide Particles via Decoration with Partial Gold Shells, *J. Colloid Interface Sci.*, 2018, **513**, 715–725.

80 A. Stevanovic, S. Ma and J. T. Yates, Effect of Gold Nanoparticles on Photoexcited Charge Carriers in Powdered TiO_2—Long Range Quenching of Photoluminescence, *J. Phys. Chem. C*, 2014, **118**, 21275–21280.

81 P. Srinoi, M. D. Marquez, T.-C. Lee and T. R. Lee, Hollow Gold–Silver Nanoshells Coated with Ultrathin SiO_2 Shells for Plasmon-Enhanced Photocatalytic Applications, *Materials*, 2020, **13**, 4967.

82 X. Pang, L. Zhao, W. Han, X. Xin and Z. Lin, A General and Robust Strategy for the Synthesis of Nearly Monodisperse Colloidal Nanocrystals, *Nat. Nanotechnol.*, 2013, **8**, 426–431.

83 X. Pang, Y. He, J. Jung and Z. Lin, 1D Nanocrystals with Precisely Controlled Dimensions, Compositions, and Architectures, *Science*, 2016, **353**, 1268–1272.

84 Y. Liu, J. Wang, M. Zhang, H. Li and Z. Lin, Polymer-Ligated Nanocrystals Enabled by Nonlinear Block Copolymer Nanoreactors: Synthesis, Properties, and Applications, *ACS Nano*, 2020, **14**, 12491–12521.

85 Y. He, Y. J. Yoon, Y. W. Harn, G. V. Biesold-McGee, S. Liang, C. H. Lin, V. V. Tsukruk, N. Thadhani, Z. Kang and Z. Lin, Unconventional Route to Dual-Shelled Organolead Halide Oerovskite Nanocrystals with Controlled Dimensions, Surface Chemistry, and Stabilities, *Sci. Adv.*, 2019, **5**, eaax4424.

86 X. Li, J. Iocozzia, Y. Chen, S. Zhao, X. Cui, W. Wang, H. Yu, S. Lin and Z. Lin, From Precision Synthesis of Block Copolymers to Properties and Applications of Nanoparticles, *Angew. Chem., Int. Ed.*, 2018, **57**, 2046.